Optimization of catalyst activity and stability in the m-cresol hydrodeoxygenation through Ni particle size control

Camila Abreu Teles [a,1], Carmen Ciotonea [b,1], Anthony Le Valant [a], Christine Canaff [a], Jérémy Dhainaut [c], Jean-Marc Clacens [a], Fabio Bellot Noronha [c,d,e], Frédéric Richard [a,*], Sébastien Royer [c,*]

[a] Université de Poitiers, CNRS, Institut de Chimie des Milieux et Matériaux de Poitiers, UMR 7285, Rue Michel Brunet, BP633, 86022 Poitiers, France
[b] Université du Littoral Côte d'Opale, Unité de Chimie Environnementale et Interactions sur le Vivant-UCEIV, UR4492, SFR Condorcet FR CNRS 3417, 59140 Dunkerque, France
[c] Université de Lille, CNRS, Centrale Lille, Université Artois, UMR 8181-UCCS-Unité de Catalyse et de Chimie du Solide, F-59000 Lille, France
[d] Military Institute of Engineering, Chemical Engineering Department, Praça Gal. Tiburcio 80, 22290-270 Rio de Janeiro, Brazil
[e] National Institute of Technology, Catalysis Division, Av. Venezuela 82, Rio de Janeiro 20081-312, Brazil

ARTICLE INFO

ABSTRACT

By taking advantage of different nanoparticle size control methodologies, the precise role of Ni particle size (from 1 nm to 9 nm) was evaluated in the HDO of m-cresol in vapor phase at 573 K under atmospheric pressure. The m-cresol HDO reaction pathways were found to be Ni-particle size dependent. The direct deoxygenation (DDO) rate increased by 10 times when decreasing Ni particle size from 9 nm to 1 nm, while the hydrogenation (HYD) and hydrogenolysis (HYG) rates moderately increased. By applying a geometric model, reaction rates were correlated to the different type of sites. Edges and corner sites (smaller particles) favor aromatics production (DDO route), while face sites (larger particles) favor both HYD and HYG routes. Catalysts partially deactivated due to coke formation, with only slight sintering observed for 1 nm Ni particles. Such findings may serve in the further preparation of active and selective catalysts for bio-oils upgrading into fuel.

1. Introduction

Pyrolysis of lignocellulosic biomass, leading to a bio-oil, is an attractive process toward the production of sustainable fuels. However, this raw bio-oil displays undesired properties such as low heating value, acidity, viscosity and high oxygen level that make it not suitable for a direct use in modern engines [1,2]. This issue can be solved by the conversion of the oxygenated compounds present in this bio-oil into hydrocarbons which are more stable and have a higher calorific value [3].

The hydrodeoxygenation (HDO) reaction can enables such conversion through a thermal treatment under hydrogen and in the presence of specific heterogeneous catalysts, the latter playing an important role to orientate the conversion of raw biomass towards selected products. In the last decades, efforts have been made to find a suitable catalyst, presenting high activity and good stability, while promoting the formation of desired deoxygenated products (benzene, toluene, xylene,

alkanes). Several catalyst formulations including sulfide and phosphide solids, transition metal oxides, and supported noble or non-noble metals have been tested for the HDO of model molecules and especially phenolic compounds such as phenol, cresol, and guaiacol, for the production of aromatics, including benzene and toluene.

Recent researches point out that bifunctional catalysts are preferred for the deoxygenation of phenolic compounds, with a metal function to catalyze hydrogenation and acidic or oxophilic sites to promote deoxygenation [4–11]. Supported noble metals such as Pt, Pd and Rh are particularly efficient for HDO reaction, however with such catalysts the favored reaction route is the hydrogenation of the aromatic ring, resulting in higher hydrogen consumption in addition to the high cost of noble metals [12–14]. The use of oxophilic supports such as ZrO_2, TiO_2 or Nb_2O_5 can promote the activation of the C-O bond and thus, combined with the properties of noble metals, favor deoxygenation [1–8,15, 16]. In the search for a compromise between efficiency and low cost for HDO reaction, supported non-noble metal (such as Fe, Co and Ni)

catalysts have also been proposed [17–22]. Especially, owing to the good hydrogenation activity of Ni at mild conditions and its slightly superior oxophilicity compared to noble metals, supported Ni catalysts are promising for HDO. Mortensen et al. evaluated the properties of different catalysts composed of different metals (Ni, Pt, Pd, Ru) and supports (SiO_2, ZrO_2, C, Al_2O_3, V_2O_5) in the HDO of phenol in liquid phase (275 °C, 100 bar) [23]. The following order of activity was found: Ni/ZrO_2 > $Ni-V_2O_5/ZrO_2$ > $Ni-V_2O_5/SiO_2$ > Ru/C > Ni/Al_2O_3 > Ni/SiO_2 > > Pd/C > Pt/C, thus demonstrating that Ni based catalysts are a promising alternative to noble metal catalysts. The best performance obtained with Ni/ZrO_2 was attributed to the activation of phenol over the support facilitating the hydrogenation over Ni particles. Thereafter, Teles et al. investigated the effect of the metal type (Pt, Pd, Rh, Ru, Ni, and Co supported on SiO_2) in the HDO reaction mechanism of phenol in gas phase [13]. Even if cyclohexanone and cyclohexanol were the main products observed, the selectivity to deoxygenated products varied according to the type of metal in the order: Ru/SiO_2 > Co/SiO_2 > Ni/SiO_2 > Rh/SiO_2 > Pd/SiO_2 > Pt/SiO_2. This same order was reported for the binding energies of atomic oxygen with the respective metal, clearly suggesting that the activity of catalysts for HDO was correlated with metal oxophilicity. Furthermore, Teles et al. studied the effect of supporting those metals over an oxophilic material such as ZrO_2 [15]. The selectivity to the deoxygenated product (benzene) was greatly improved over Ni/ZrO_2 catalyst as compared to the noble-metal based catalysts (selectivity to benzene of 26.7 % over Ni/ZrO_2 against to 0.8 %, 3.3 % and 3.1 % for Pt/SiO_2, Pd/SiO_2 and Rh/SiO_2 catalysts, respectively). Moreover, the addition of a secondary oxophilic metal such as Fe is reported to improve the HDO ability of Ni-based catalysts [19,24–26]. Nie et al. investigated the selective conversion of m-cresol on SiO_2 supported Ni, Fe and bimetallic NiFe catalysts in gas phase [24]. They found oxygenated and transalkylation compounds as the main products over Ni/SiO_2 catalysts (33.3 % of selectivity to 3-methylcyclo-hexanone, 11.1 % to 3-methylcyclohexanol and 24.8 % to trans-alkylation products), while toluene is dominant over Fe and $NiFe/SiO_2$ (52.6 % of selectivity to toluene and 45.3 % to transalkylation products). Other bimetallic combinations including NiMo [27,28] and NiCo [22] have also been evidenced to present improved deoxygenation ability for the HDO of phenolic compounds. As mentioned above, another way to improve the activity of Ni-based catalysts is the selection of support as it affects Ni dispersion, and it can provide acidic and/or oxophilic sites orientating the activity and selectivity during reaction. Thus, Ni deposited on oxophilic Nb_2O_5 support was found to be highly selective for the deoxygenation of phenol, with 97 % of selectivity to benzene. Song et al. also reported higher activity for the deoxygenation of phenol in liquid phase using Ni deposited on an acidic zeolite H-ZSM-5 support when compared with a Ni/SiO_2 catalyst (TOF of deoxygenation: 769 and 127 h^{-1} for Ni/HZSM-5 and Ni/SiO_2 respectively) [29].

Besides the nature of support, the effect of the support pore structure and the metal particles size over the HDO reaction have received far less attention. In the most of the studies, the effect of metal particles size is evaluated by employing bifunctional catalysts, in which the support properties such as acidity, oxophilicity and/or presence of oxygen vacancies may also influence the reaction mechanism [15,16,30–36]. Then, a systematic investigation of catalysts by varying metal particles size and eliminating the influence of support, is needed. Yang et al. have conducted an interesting study on the effect of Ni particles (2–22 nm) supported on SiO_2 for the HDO of m-cresol in gas phase and observed that decreasing Ni particles size from 22 to 2 nm increased the TOF of m-cresol conversion by 3 times as well as favored the deoxygenation pathway [37]. The TOF for deoxygenation (yielding toluene) increased 6 times from Ni 22 nm (0.008 s^{-1}) to 2 nm (0.0478 s^{-1}) while hydro-genolysis (yielding phenol and CH_4) was decreased by 2.6 times (from 0.052 to 0.0197 s^{-1}). Comparable findings were obtained by Mortensen et al. in the HDO of phenol at liquid phase [38]. The effect of support pore structure was investigated by Vargas-Villarán et al. by testing Ni catalysts supported on SBA-15 and protonated titanate nanotubes in the

HDO of anisole [39]. Several methods of Ni incorporation were applied to vary the dispersion of Ni particles. Over SBA-15 supported catalysts, hydrogenation of the aromatic ring yielding cyclohexyl-methyl-ether was the main reaction pathway, the formation of this product being favored over larger Ni particles (45 % and 37 % of yields over Ni particles of 17 and 3 nm, respectively). The selectivity to deoxygenated products (sum of benzene, cyclohexene and cyclohexane) was improved over smaller Ni particles (4.6 % over Ni 17 nm compared with 20 % over 3 nm particles). Thus, tuning the catalyst properties by combining small metal particles inside a well-structured support may be a promising strategy to design efficient and low-cost catalysts for the HDO of the bio-oil. It is also important to note that, the influence of metal particle size in the stability of catalysts is rarely investigated. For instance, metal sintering and/or blockage of the active sites by coke are the main causes of catalyst deactivation during the HDO reaction and thus, the stabilization of those small particles is desired.

In this point of view ordered mesoporous silicas such as SBA-15 are interesting supports owing to their high specific areas, narrow pore size distribution and large pore volume. The ordered channel-type mesopores, wider pore sizes and thicker pore walls allow the accommodation of larger reactants and permit to control the catalyst particle size [40, 41]. Furthermore, confining metal particles in the mesopore channels or secondary micropores of SBA-15 support may contribute to the stabilization of metal particles avoiding sintering, which is one of the major reasons for catalyst deactivation in the HDO reaction.

In the present work we investigated the effect of the support pore structure by comparing conventional silica and SBA-15 materials and the effect of Ni metal particles size in the HDO reaction of m-cresol. We proposed different synthesis approaches in order to finely control and stabilize Ni nanoparticles on the SBA-15 pore structure: deposition-precipitation with urea (DP) and melt infiltration (MI). The materials were characterized after calcination and reduction, and relationships between particle size and product selectivity, as well as catalyst deactivation, were established. A geometric model was also developed to quantify the surface site concentration according to the Ni particles size and confronted with the catalytic results. A good correlation was obtained thus providing a simpler and efficient tool to predict the structure-activity relationship and determine the nature of active sites in the HDO reaction.

2. Experimental section

2.1. Materials

All chemicals required to prepare the mesoporous SBA-15 and the NiO containing materials were used as received: $Si(OC_2H_5)_4$ (TEOS, 98 wt%, Sigma-Aldrich), non-ionic triblock copolymer Pluronic P123 (poly (ethylene oxide)-block-poly(propylene oxide)-blockpoly(ethylene oxide)-block, $PEO_{20}PPO_{70}PEO_{20}$, MW = 5800, BASF Corp. Sigma Aldrich), hydrochloric acid (HCl, 37 wt%, Sigma-Aldrich), nickel nitrate ($Ni(NO_3)_2 \cdot 6H_2O$, Sigma-Aldrich), urea ($CO(NH_2)_2$ > 99.0 wt%, Sigma-Aldrich, ACS reagent).

2.2. Support preparation

Two silica-based supports were used in this work: commercial SiO_2 (Aerosil 300) and an ordered mesoporous SBA-15. The SBA-15 support was synthesized by using an experimental protocol previously described [42]. The polymer P123 (4 g), was dissolved at 40 °C under acidic conditions (150 mL of 1.6 M HCl) and stirring. Then, the silicon source, TEOS (8.5 g), was added dropwise and the mixture was kept for 24 h under constant stirring at the temperature of 40 °C. Then, a hydro-thermal treatment was performed at 100 °C for 48 h. The solid was recovered by filtration and washed with water before being dried for 24 h at 100 °C. Template elimination was performed by calcination at 550 °C for 6 h (in a muffle furnace, using a heating ramp of 1.5 °C min^{-1}),

producing a support designated as SBA.

2.3. Catalyst preparation

Ni supported on SiO_2 was prepared by incipient wetness impregnation (IWI) of the support with nitrate precursor ($Ni(NO_3)_2.6H_2O$) solution. The corresponding aqueous metal nitrate precursor solution (0.04 mol L^{-1}) was prepared in order to obtain 10 wt% of Ni onto the support. The solution was dropwise added to the dried support, until a homogenous paste is obtained. The solid was thereafter dried under air at 25 °C during 5 days. The powder was then calcined under air at 400 °C for 5 h (heating ramp of 1.5 °C min^{-1}). This material was denoted 25nmNi/SiO_2.

Ni supported on SBA-15 samples were prepared by Melt Infiltration (MI) method in order to obtain different Ni particles sizes [43]. To reach Ni nanoparticles sizes of around 9 nm, the precursor $Ni(NO_3)_26H_2O$ was incorporated into the calcined SBA-15 by gentle grinding at ambient conditions for 30 min according to a previously reported method [43]. The powder was then treated in a teflon autoclave at the melting point of the precursor (57 °C) during 3 days, and the solid was further calcined at 500 °C for 6 h (heating ramp of 1.5 °C min^{-1}). To obtain Ni nanoparticles of around 1 nm, the same method was used, excepted that a non-calcined SBA-15 support (thus containing the polymer pluronic P123 within the silica) was used and subjected to a thermal treatment at 57 °C during 4 days.

SBA-15 loaded with Ni nanoparticles of around 3 nm was prepared by the deposition-precipitation-urea (DP) method [44], allowing to incorporate nickel within layers of a phyllosilicate phase. The synthesis was performed in a thermostated reactor (V = 250 mL), by using 1 g of SBA-15 as silica source. A precise quantity of the nickel precursor, Ni $(NO_3)_26H_2O$ equal to obtain 10 wt% of Ni, was dissolved in 70 mL of H_2O and added to the water solution containing the SBA-15. A solution of urea (3 mol L^{-1}) was thereafter used (1 mol of NH_3 for each mol of nitrate used for the synthesis). When the temperature of the suspension was stabilized at 90 °C, the urea solution was added dropwise and the stirring was maintained for 24 h. Under these conditions, the release of ammonia into the solution unfolds slowly, allowing enough time to a slow and controlled crystallisation of the phyllosilicate at the surface of the SBA-15 grains. At the end of the ageing step, the pH measured was of 7.4 ± 0.1. The Ni-containing solid, recovered by filtration, was washed with deionised water before being dried at 40 °C during 12 h. The prepared material was finally calcined in a muffle oven at 500 °C for 6 h, with a heating rate of 1.5 °C min^{-1}.

The prepared Ni-containing solids were denoted as XnmNi/SBA-15, where "X" refers to the average particle size (9, 3 and 1 nm).

2.4. Catalyst characterization

Ni loading was determined by inductively coupled plasma optical emission spectroscopy (ICP-OES) on a SPECTRO ARCOS ICP-OES instrument. Before analysis, the samples were digested using concentrated nitric acid and hydrofluoric acid on a microwave heating system.

Textural properties were determined by N_2-physisorption. Isotherms were recorded at − 196 °C on a Micromeritics Tristar II Plus apparatus. Before analysis, the samples were outgassed under dynamic vacuum at 350 °C for 3 h in order to remove any traces of water or impurities. Values were calculated using Tristar II software version 4.06. Specific surface area was determined using the multipoint B.E.T. algorithm in the p/p_0 range from 0.10 to 0.25. The mesopore size distribution was determined using the B.J.H. equation applied to the desorption branch [45,46]. Pore volume is determined at $p/p_0 = 0.98$, on the adsorption branch. The micropore surface and microporous volume were determined by t-plot method.

Crystalline phase formation was analysed by X-ray diffraction (XRD), performed on the powder samples, using a Bruker D8 Passeur X-ray diffractometer in Bragg-Brentano geometry configuration. XRD patterns in the wide-angle range were recorded with Cu Kα radiation (λ = 0.154 nm) in the 10–80° 2θ range with a step size of 0.05° each 2 s. Phase identification was made by comparison with the ICDD database.

In-situ XRD under H_2 was performed to investigate the evolution of the phases. The analyses were also conducted on the same X-ray diffractometer equipped with a VANTEC-1 detector. Kanthal (FeCrAl) filament cavity was used for analysis. The Kanthal gives two intense peaks at 2θ = 43.57° and 63.87°, which were not taken into consideration for the interpretation of the diffractograms. The reduction conditions used were: 30 mL min^{-1} of 3.0 vol% H_2 in He in the range of temperature from 30 °C to 700 °C (rate = 10 °C min^{-1}). The diffractograms were recorded in the 2θ range between 10° − 80° with a step size = 0.05° and step time = 2 s

Morphology and dispersion state in the samples were analysed by transmission electron microscopy (TEM) using a JOEL 2100 UHR equipment, operated at 200 kV, with a LaB_6 source and equipped with a Gatan Ultra scan camera. The samples were first embedded in a polymeric resin, sliced into 50 nm-thick sections using an ultramicrotome and then deposited on a carbon grid for analysis. HRTEM images were recorded over the reduced samples and the post HDO reaction catalysts. For the reduced samples, the reduction was carried out under pure H_2 flow (50 mL min^{-1}) at 700 °C during 2 h. The software ImageJ version 1.8 was used to analyse the images and to plot particle size histograms.

X-ray photoelectron spectroscopy (XPS) analysis was used to evaluate the surface composition of the calcined and reduced samples. The analyses were performed on a Kratos Axis Ultra DLD spectrometer, using monochromatic Al Kα radiation (1486.7 eV), operating at 150 W (15 kV and 10 mA). To avoid charge effects, a charge neutraliser was operated during analysis. Binding energies (BE) were referred to the C 1 s line of carbon contaminant at 284.8 eV with an uncertainty of ± 0.1 eV. High-resolution spectra were collected at a step of 0.1 eV (pass energy, 20 eV). The calcined samples were pressed in a hollow stub and loaded into a high vacuum chamber ($\leq 9\ 10^{-8}$ Pa). Reduction was carried out in a catalysis chamber coupled to the spectrometer and transferred in high vacuum without contact with the atmosphere. During reduction, the samples were heated to 500 °C, 5 °C min^{-1}, during 1 h under a 50 mL min^{-1} flow of pure H_2. Afterwards, the samples were cooled under H_2, and degassed prior to being transferred to the analysis chamber ($\leq 9\ 10^{-8}$ Pa). Fitting and deconvolution were achieved with CasaXPS software (version 2.3.24), applying Gaussian/Lorentzian function (30 % Lorentzian) and added asymmetry parameters for metallic Ni2p.

Activation of oxide precursors was studied by temperature-programmed reduction under H_2 (H_2-TPR). Experiments were conducted on an Autochem II chemisorption analyser (Micromeritics), equipped with a TCD. The consumption of H_2 was derived from the TCD signal, after calibration. Before a H_2-TPR run, the solid was heated at 500 °C under 50 mL min^{-1} of air flow (10 °C min^{-1}) during 1 h. After cooling down to room temperature, the H_2 containing flow was stabilized (50 mL min^{-1}, 5.0 vol% H_2 in Ar) and the temperature-programmed reduction was performed (from 25 °C to 900 °C, with a temperature ramp of 5 °C min^{-1}).

CO chemisorption analysis was performed to estimate the metallic dispersion and calculate TOF values. The samples were firstly reduced at 500 °C (5 °C min^{-1}), under pure hydrogen flow (30 mL min^{-1}) for 1 h. The reactor was then cooled down to the adsorption temperature (30 °C) under helium (30 mL min^{-1}) and successive pulses of pure CO (0.465 mL) were injected each 3 min. Results were collected by a gas phase chromatograph equipped with a TCD detector and a Porapak Q column, allowing the quantification of CO chemisorbed.

The acidity of the catalysts was measured by DRIFTS of adsorbed pyridine. Experiments were conducted on a Nicolet Nexus instrument equipped with a DTGS detector and a quartz cell with CaF_2 windows. The samples were first reduced at 500 °C under pure flow of hydrogen for 1 h. Then, the samples were cooled down to 150 °C, and a spectrum of the sample was registered as reference. Pyridine adsorption was carried out during 5 min, with a further vacuum purge during 1 h.

Spectra were recorded between 150 and 450 °C at a resolution of 2 cm^{-1} and accumulating 64 scans bet.

Thermogravimetric analysis coupled with a mass spectrometer (TGA-MS) was performed over the spent catalysts in order to investigate the deposition of carbon over the catalysts during the HDO reaction. The measurements were carried out on a SDT Q600 TA Instruments apparatus coupled by a heated capillary column with a QGA mass spectrometer from Hiden. The analysis was performed in the temperature range of 25 °C up to 1000 °C, 10 °C min^{-1}, under flow of 100 mL min^{-1} of synthetic air.

2.5. HDO of m-cresol

Vapor phase HDO reaction of m-cresol was conducted in a fixed-bed flow reactor system, operating at 300 °C under atmospheric pressure. The carrier gas flow rate was 50 mL min^{-1} of H$_2$ and a H$_2$/m-cresol molar ratio was fixed at 90. Preliminary calculations (Weisz-Prater criteria, see supplementary information file) and tests were carried out following the same criteria proposed by Madon and Bourdart [47] to ensure no internal and external mass transfer limitations. Before the reaction, the catalysts were reduced in situ under pure hydrogen (50 mL min^{-1}) at 500 °C (5 °C min^{-1}) for 1 h. The reactant feedstock was introduced at the top of the reactor by using a push-syringe. The feedstock was composed by m-cresol as the reactant (7 mol%), n-heptane as an internal standard (3 mol%) and dodecane as the solvent. The different catalysts were tested at different W/F values, which is defined as the catalyst weight (in g) divided by the molar flow rate of m-cresol (in mol h^{-1}), by changing the catalyst weight, in order to obtain comparable levels of conversion. The line at the reactor outlet was maintained at 5 °C using a circulator Huber minichiller in order to condense any unconverted reactant and products. The first liquid sample was taken after 0.5 h and analysed by a Varian 430 chromatograph equipped with a DB-5 capillary column and a flame-ionization detector (FID). The conversion of m-cresol and product selectivity for each product were calculated using Eqs. (1) and (2):

$$X(\text{in \%}) = \frac{n^0_{m-cresol} - n_{m-cresol}}{n^0_{m-cresol}} \times 100 \tag{1}$$

$$S_i(\text{in } mol\%) = \frac{n_i}{n^0_{m-cresol} - n_{m-cresol}} \times 100 \tag{2}$$

Where $n^0_{m-cresol}$ and $n_{m-cresol}$ are the number of moles of m-cresol initially and after 0.5 h of reaction, respectively; n_i is the number of moles of a given i product.

Assuming a pseudo-first-order reaction rate, the total kinetic rate constant (k_{TOT} in mmol g$_{Ni}^{-1}$ h^{-1}) and the kinetic rate constants for the different reactions pathways were calculated using the Eqs. (3) and (4):

$$k_{TOT}(\text{in mmol } g_{Ni}^{-1} h^{-1}) = \frac{-F.Ln(1-X)}{w.(\%Ni)} \tag{3}$$

$$k_y(\text{in mmol } g^{-1} h^{-1}) = r_{TOT}.S_y \tag{4}$$

Where k_{TOT} is the total kinetic rate constant determined for the global transformation of m-cresol and k_y are the kinetic rate constants for the different reaction pathways, X is the m-cresol conversion, F is the m-cresol molar flow rate (in mmol h^{-1}), w is catalyst weight (in g), %Ni is the Ni content measured by ICP-OES and S_y is the selectivity to the different products: toluene for the deoxygenation route (DDO), 3-methylcyclohexanone, 3-methylclyohexanol, methylcyclohexene isomers and methylcyclohexane for the hydrogenation route (HYD), phenol and benzene for the hydrogenolysis route (HYG).

The turnover frequency (TOF, in h^{-1}) values were estimated using the Eq. (5):

$$TOF = k_y/M$$

Where k_y is the kinetic rate constant for the different reaction

pathways and M is the CO uptake (in mmol g^{-1}) obtained from chemisorption measurements.

3. Results and discussion

3.1. Catalyst characterization

All catalysts, excepted 3nmNi/SBA, presented Ni contents close to the expected values, i.e. 8.1–9.7 wt%. In the case of 3nmNi/SBA, a lower loading, i.e. 5.7 wt%, was measured. This result originates from the deposition-precipitation method used for the synthesis. At pH of 7.5, part of the Ni precursor remains in the synthesis solution in the ionic form, leading to a lower loading than expected in the final material. This is however not problematic for the comparison with the other catalysts since reaction conditions (i.e. the mass of catalyst in the reactor) is adjusted to obtain comparable conversions for all catalysts.

Wide-angle XRD (Fig. 1) was used to obtain structural information on the calcined samples. For 25nmNi/SiO$_2$, 9 nmNi/SBA and 1nmNi/SBA samples, the diffractograms showed the main reflections positioned at 37°, 43° and 62° which are associated with the formation of a NiO crystalline phase, by comparison with the ICDD database (cubic structure, PDF file n° 47-1049). The reflections intensity and width vary over the different catalysts, indicating that different NiO average crystallites sizes were obtained by changing the synthesis route. The narrow width
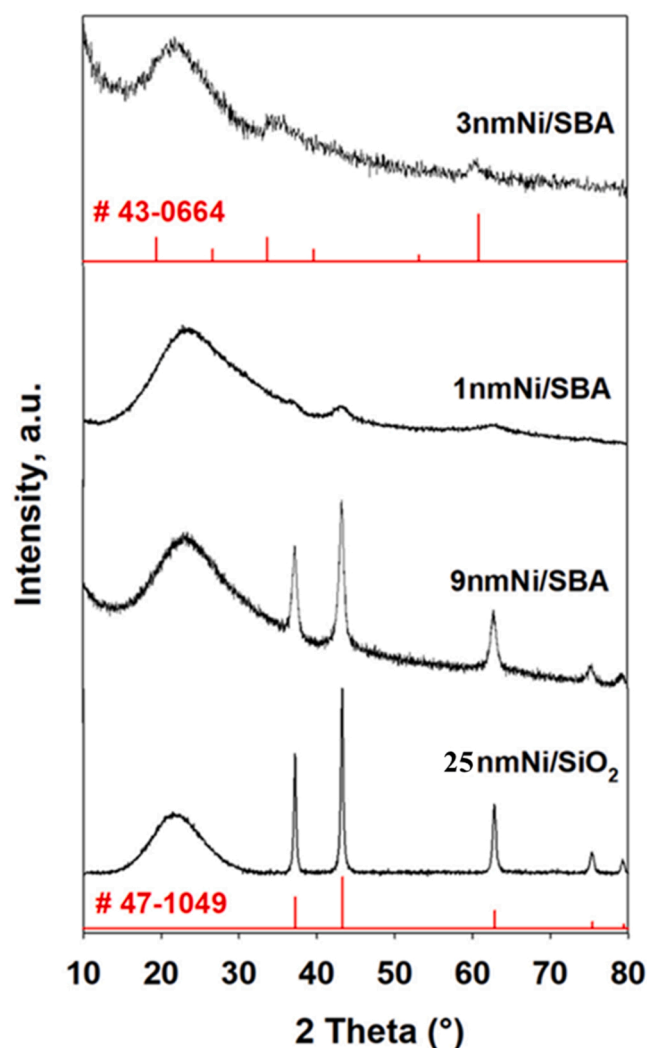

Fig. 1. Wide-angle XRD for calcined Ni containing materials. In red ICDD files of Ni 1:1 phyllosilicate (pdf: 43-0664) and NiO (pdf: 47-1049).

of the diffraction lines in the 25nmNi/SiO₂ and 9nm/SBA samples indicate the formation of large NiO particles while for 3nmNi/SBA and 1nmNi/SBA, the low intensity or absence of lines indicates the formation of much smaller crystallites. The XRD pattern of 3nmNi/SBA sample completely differs, since a broad and low intensity lines at 35° and 60° is observed. It clearly indicates the formation of nickel 1:1 phyllosilicate (kerolite phase, ICCD reference n° 43-0664), as expected at the issue of the deposition-precipitation procedure. NiO average crystallite sizes, deduced from XRD patterns applying the Scherrer equation, after Warren's correction of instrumental broadening, leads to values of 21 nm for the shaper signals obtained for the 25nmNi/SiO₂ sample, 9.2 nm for 9nmNi/SBA and < 2 nm for the 1nmNi/SBA sample (Table 1). As expected, the use of the melt infiltration procedure over calcined SBA-15 leads to mesopore confined NPs of transition metal oxide (∼ 9 nm), while the use of the porogen containing support leads to intra-wall pore immobilized NPs, hardly detected by XRD [43,48]. Finally, the DP approach induces the formation of a phyllosilicate phase without any detectable formation of individual NiO crystalline phase.

To investigate the stability of the small Ni particles in the 3nmNi/SBA and 1nmNi/SBA samples, XRD patterns during in situ reduction (30–700 °C) are showed in Fig. S1. For the 1nmNi/SBA sample, in which it is possible to observe large humps attributed to the NiO, the initially visible reflections disappear above 400 °C and are replaced by broad lines corresponding to the Ni metallic phase (PDF file 04-0850). For the 3nmNi/SBA sample, reflections are never observed indicating that Ni(0) particles remained too small onto support, or amorphous, after catalyst reduction even if the reduction is performed up to 700 °C. These results show the higher resistance to sintering of these catalysts when subjected to high temperature treatments.

The textural properties of the calcined samples were evaluated by N₂ physisorption. The adsorption/desorption isotherms are presented in Fig. 2, while the extracted quantitative information are presented in Table 1. Commercial SiO₂ exhibited a type IV isotherm, with a H3-type hysteresis indicating the presence of mesopores with a broad distribution of pore diameter. The bare support presented a B.E.T. area (S_{BET}) of 301 m² g⁻¹ and an average pore size of 13.5 nm. When Ni is impregnated onto the silica, the S_{BET} and pore size dropped to 242 m² g⁻¹ and to 9.3 nm respectively. We associate this modification of the textural properties to the presence of Ni NPs inside the porosity of the silica. For the parent SBA-15 support as well as the 9nmNi/SBA and 1nmNi/SBA samples, typical type IV(a) isotherms with H1-type hysteresis were observed. Such isotherms with parallel adsorption/desorption branches are associated to materials having cylindrical pores, positioned in the mesopore domain as indicated by p/p₀ from 0.55 to 0.66–0.77 [43]. For
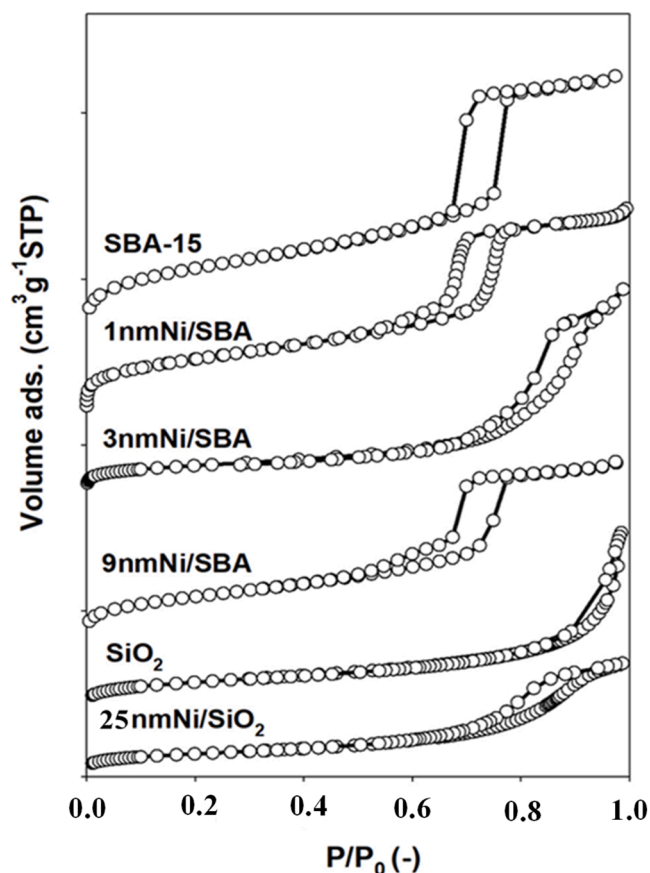

Fig. 2. Adsorption/desorption isotherms for calcined materials.

the 9nmNi/SBA and 1nmNi/SBA samples, prepared by melt infiltration method, a latency is observed for the closure of the desorption branch of hysteresis, being more evident for the 9nmNi-SBA catalyst, which is related to the formation of NPs (NiO) inside the tubular pores and leading to constrictions (1nmNi/SBA) and constrictions plus pore plugging (9nmNi/SBA). The presence of confined NiO nanoparticles causes the so called "ink-bottle" shape porosity, which also induces sensible decrease of specific surface areas and pore volumes due to the partial blockage of mesopores access.

For these catalysts prepared by melting infiltration method, a

Table 1
Textural properties, reduction degree and average particle size of the Ni-based catalysts.

Sample	Ni wt%	N₂ physisorption				Red. T.[e] (°C)	Degree of red. (%)	d_{Ni}[f] (nm)	% Atoms at NP surface[g]	D_{Ni}[h] (%)
		S_{BET}[a] (m² g⁻¹)	S_{μ}[b] (m² g⁻¹)	V_p[c] (cm³ g⁻¹)	D_p[d] (nm)					
SiO₂	-	301	-	0.43	13.5	-	-	-	-	-
SBA-15	-	820	207	1.25	8.4	-	-	-	-	-
25nmNi/ SiO₂	9.7	242	-	0.47	9.3	401; 482	100	25 (21)	16.7	4
9nmNi/SBA	9.5	511	59	0.91	6; 8.4	404; 593	91	7.7 (9.2)	20.6	8
3nmNi/SBA	5.7	306	39	0.18	8.5–15	622	93	3.5	33.3	24
1nmNi/SBA	8.1	579	28	0.91	6.7	547	83	1.2 (< 2)	62.5	28

[a] S_{BET} specific surface calculated with BET equation;
[b] S_{μ} microporous surface with t-plot;
[c] V_p pore volume at P/P₀ = 0.98;
[d] D_p average pore diameter calculated with BJH on desorption method;
[e] Maximum peak temperature recover from the TPR profiles;
[f] Average particles size calculated from TEM images of the reduced catalysts by using ImageJ software. In parentheses the values deduced from the XRD applying the Scherrer equation;
[g] % of atoms exposed on the surface, calculated using the particle sizes determined by TEM statistical analysis, considering that $d_{Ni} = 0.84 \times d_{NiO}$ based on the differences of molar mass and density, and that for each particle, Ni dispersion (%) = 97.1/d_{Ni} (nm).
[h] Ni dispersion measured by CO chemisorption.

decrease in the surface area is observed after Ni infiltration (area decreased from 802 m^2 g^{-1} of the parent support SBA-15 to 511 m^2 g^{-1} for 9nmNi/SBA and to 579 m^2 g^{-1} for 1nmNi/SBA). Additionally, an important decrease in the microporous area is observed for 1nmNi/SBA (decrease of 86 % by comparing to the initial microporous area of the parent SBA-15). This was previously reported by Chen et al. and it was assumed to originate from the specific localization of small Ni nanoparticles located inside the secondary microporosity (intra-wall pores) developed by the SBA-15 support when synthesized at temperature of ~ 100 °C [49].

For the 3nmNi/SBA sample, a type IVa isotherm with a H2(b)-type hysteresis is observed. It indicates the presence of mesopores with heterogenous size and shape that are formed during the deposition precipitation synthesis process. During the synthesis, silica partially solubilized and reprecipitated in the form of phyllosilicate plate-like particles [48]. As a consequence, the surface area dramatically decreased to 306 m^2 g^{-1} (−63 % when compared to the SBA-15). The significant shift of the adsorption and desorption steps toward the higher p/p$_0$ indicates the formation of large disordered mesopores which replace the highly ordered mesoporosity of the initial SBA-15 during the dissolution-reprecipitation process. The mesoporosity is however partially maintained, with a broad range of pore size measured (9–15 nm).

Information on the pore architecture of SBA-15 support as well as on the location and size of Ni particles were assessed from HRTEM images of the reduced catalysts and are shown in Figs. 3 and S2. For the 25nmNi/SiO$_2$ catalyst, it is clearly observed the presence of large Ni nanoparticles (average of 25 nm) in accordance with the value obtained from XRD of the calcined catalyst. For the 9nmNi/SBA catalyst, the presence of Ni nanoparticles in the range of 8–9 nm confined within the mesopores of SBA-15 is observed. For the 1 nmNi/SBA catalyst, the formation of significantly smaller Ni nanoparticles, about 1 nm in the pores of SBA-15, is detected. This last result confirms the efficiency of the melting infiltration method when maintaining the P123 porogen inside SBA-15 to control the localization of the nickel nitrate precursor before its thermal decomposition for oxide formation. We previously proposed that the diffusion of the nitrate precursor at the hydrophilic interface between silica and P123 occurs, and that the nitrate precursor will be stabilized into the secondary intrawall micropores of the SBA-15 due to their higher silanol density. Then, after stabilization and reduction, Ni(0) particles are observed to be physically stabilized (confined) in this secondary – low size – porosity [36].

In the case of 3nmNi/SBA catalyst, obtained via deposition-precipitation method, the formation of the phyllosilicate phase is confirmed by the observation of filaments inside and outside of the SBA-15 grains. As can be seen in Fig. S2, large phyllosilicate filaments are mainly located at the external surface of the SBA-15, with some observed to grow separately from the silica grain surface. The phyllosilicate growth is expected though the dissolution - reprecipitation mechanism proposed by Burratin [50] in which the adsorption of hexacoordinated Ni cations onto the brucitic layer of Si(OH), lead to the formation of a metallic layer, in contact with the silica surface. After increase in the pH of the synthesis solution, the silica dissolves with the formation of a phyllosilicate phase. These successive steps are determining to efficiently incorporate the Ni(II) cations inside the crystalline phase, and to *in fine* obtain an efficient stabilization of the Ni(0) nanoparticles after reduction of the phyllosilicates. Regarding the structure of SBA-15, cavities can be observed through the silica, together with lamellar segments inside the silica grain which are formed after reduction of the catalyst (Fig. S2). This also confirms the stabilization of mesopores, as deduced from N$_2$ physisorption analysis. The Ni particle sizes obtained in this catalyst are comprised between 2 and 5 nm (average of 3.5 nm).

The dispersion of the Ni nanoparticles on the materials was accessed by CO chemisorption measurements (Table 1). As expected, Ni dispersion significantly varied between the catalysts, following the order: Ni/

SiO$_2$ (4 %) < 9nmNi/SBA (8 %) < 3nmNi/SBA (24 %) < 1nmNi/SBA (28 %). These values show that Ni(0) accessibility increases in the same order that Ni nanoparticles size (measured by TEM) decrease. These results demonstrate that, despite the confining phenomenon, the 1 nm Ni particles remain accessible to gas and liquid reactants, as confirmed by previous studies performed in hydrogenation [36].

The reducibility of Ni-based catalysts was evaluated by H$_2$-TPR and the profiles are presented in Fig. 4. For the 25nmNi/SiO$_2$ sample, a main peak at T$_{max}$ of 401 °C is observed that is attributed to the presence of bulky NiO particles. For the 9nmNi/SBA catalyst, it is also observed a reduction of bulky NiO nanoparticles, probably located close to the external surface of SBA-15 (T = 404 °C). A second reduction peak at higher temperature (593 °C) is observed, and it can be likely due to the reduction of confined nanoparticles inside the mesopores. The higher reduction temperature in this case can be associated with the presence of the multiple chained nanoparticles in the same pore, reducing the rate of reduction through diffusion process. For the 1nmNi/SBA catalyst, only one peak is observed at 547 °C which is ascribed to the reduction of homogeneous NiO nanoparticles of low size confined into the pores. The broad shape of this peak indicates the presence of nanoparticles hardly accessible to the reduction, which is in agreement with the specific localization of these particles, inside the intra-wall microporosity of the SBA-15, as previously discussed [36]. For the 3nmNi/SBA sample, reduction occurs at higher temperature, with a broad peak located at 622 °C. This temperature is characteristic of the reduction of the Ni cations incorporated inside phyllosilicate phase, as previously demonstrated by Burratin [50]. Therefore, the obtained result demonstrates that the use of the SBA-15 as silica source and the mild basic media obtained by the decomposition of the urea lead to an almost complete incorporation of Ni(II) cations inside the phyllosilicate, as evidenced by the presence of a single reduction step, and the formation of very minor external – bulk NiO particles (visible by a very small H$_2$ consumption at 246 °C). The degree of reduction calculated according to the consumption of H$_2$ is reported in Table 1, showing a complete reduction of Ni when supported on silica and from 83 % to 93 % when supported on SBA-15.

The nickel speciation over the catalysts surfaces after activation at the same conditions used before the catalytic reaction (i.e., 500 °C, pure flow of H$_2$ for 1 h) was determined by XPS analysis. All spectra were positioned using the Si 2p signal located at 103.5 eV. The spectra of Ni 2p 3/2 core level for the samples after activation are presented in Fig. 5. After in situ reduction at 500 °C, a signal is observed around 852 eV, corresponding to the Ni 2p3/2 signal which indicates the presence of Ni (0). However, signals characteristic of Ni(II), in the form of Ni(OH)$_2$ or eventually silicate, is still observed for the supported catalysts indicating that nickel is not completely reduced under the used conditions. Table 2 shows the fraction of Ni(0) and Ni(II) at the surface of the reduced samples. The percentage of Ni(0) was 60 % for the 25nmNi/SiO$_2$ catalyst and 55 % for 9nmNi/SBA. Over the series of SBA-15 supported catalysts, the fraction of Ni(0) decreases by decreasing Ni particle size with only 39 % of Ni being reduced to metal at 500 °C for the 1 nm/SBA catalyst. This confirms the results previously obtained by TPR-H$_2$ and showing a decrease of Ni(II) cation reducibility over the low particle size samples.

Pyridine adsorption-desorption DRIFTS experiments were performed on the reduced catalysts in order to determine catalyst acidity. The total acidity and acidic site distribution are listed in Table 2. Ni/SiO$_2$ catalyst did not show noticeable acidity, in agreement with previous works [51]. For the series of Ni supported on SBA-15 catalysts, bands associated to pyridine adsorbed on Lewis acid sites at 1456 and 1624 cm^{-1} were observed, and the values of acidity varied between 16 and 38 μmol g^{-1}. This is probably related to the presence of non-reduced NiO species, as observed by XPS analysis of the reduced samples.

3.2. Evaluation of the catalysts in the HDO reaction of m-cresol

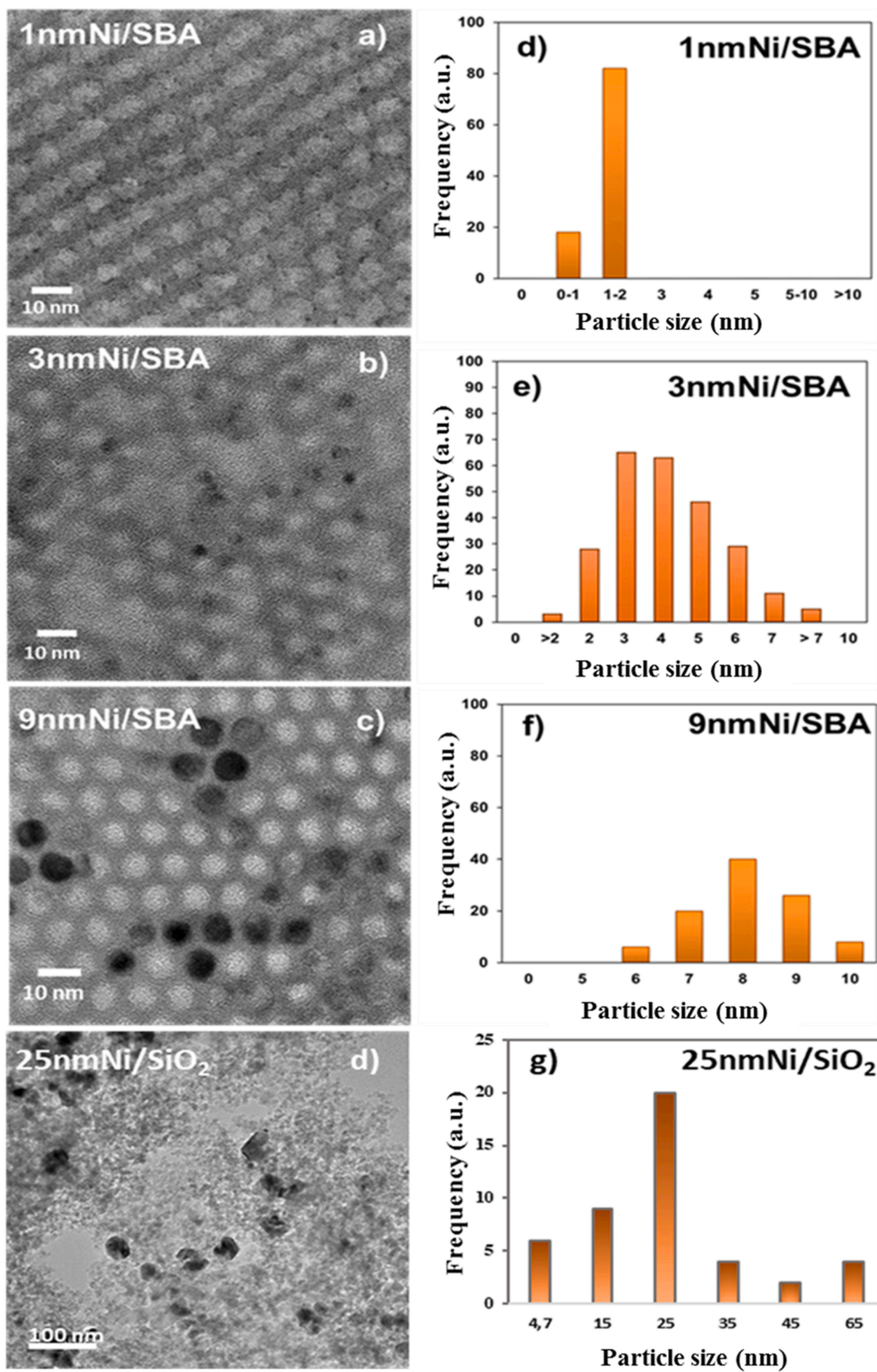The HDO of m-cresol was performed at 300 °C under atmospheric

Fig. 3. Representative HR-TEM images and the respective histograms recovered onto multiple images for the Ni-based catalysts in the reduced form.
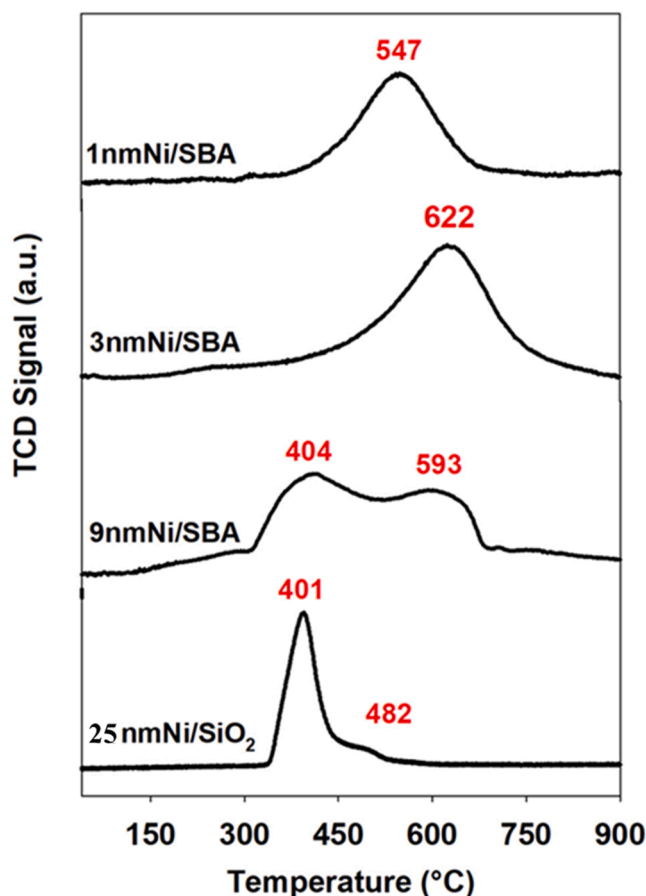
Fig. 4. TPR profiles for calcined Ni containing materials.

pressure. The reaction was carried out at different space times in order to obtain similar levels of conversion (around 25 %) for all catalysts. Table 3 shows the product distribution obtained during the conversion of m-cresol after 0.5 h of time on stream (TOS). In all cases, toluene (TOL) is always the main product, its selectivity varying between 46 and 86 mol% depending on the catalyst used. The other major products are methylcyclohexanone (m-ONE) and phenol (Ph), with minor amounts of methylcyclohexanol (m-OL), methylcyclohexenes (m-ENES), methyl-cyclohexane (m-ANE) and benzene (Bz).

Based on the product distribution observed in the present work and on the previous works that performed HDO of m-cresol of similar phenolic compounds such as phenol at similar reaction conditions over metal supported catalysts [8,13,24,37], the main reaction routes involved in the transformation of m-cresol over Ni supported catalysts are depicted in Scheme 1. The reaction proceeds via three main parallel pathways: (i) Direct deoxygenation (DDO) producing toluene which may proceeds via the direct cleavage of C-O bond or by involving the formation of an tautomer intermediate; (ii) hydrogenation (HYD) of the aromatic ring leading to the formation of oxygenates such as 3-methyl-cyclohexanone and 3-methylcyclohexanol, which may be further dehydrated to form methylcyclohexenes, followed by its hydrogenation to methylcyclohexane and (iii) hydrogenolysis (HYG) with the cleavage of the methyl group of m-cresol yielding phenol and methane, the former being mainly deoxygenated into benzene by the same reactions routes proposed for the deoxygenation of m-cresol to toluene. Assuming that methane comes mainly from hydrogenolysis of the methyl group of m-cresol and no transalkylation products were observed, we assume that the methane/phenol molar ratio has to be close to one.

It is important to note that the contribution of each reaction pathway varies with the type of catalyst, depending on several parameters such as the nature of the metallic phase and the support used. For example, a

highly oxophilic metal such as Ru or Fe is able to carry out the direct cleavage of the C-O bond due to the strong energy bond of these metals with the oxygen atom, thus weaking the C_{Ar}-O bond and favoring the DDO route. Less oxophilic metals, such as Pd, Pt, and Ni, have a tendency to promote the HYD route toward the ketone as a major product. In this case, the tautomerization of m-cresol has been proposed as the initial step [13,31,52]. The formation of a tautomer intermediate allows the deoxygenation by the hydrogenation of the carbonyl bond which involves a lower energy barrier. Thus, metals such as Ni and Co which present intermediate oxophilicities [binding energy with atomic oxygen (eV): Pt(−4.20) < Pd(−5.04) < Rh (−5.04) < Ni(−5.40) < Co(−5.58) < Ru(−5.90)] may promote deoxygenation to some extent [53]. Then, in the present work, we propose the DDO and HYD to happen starting from the tautomerization of m-cresol over the Ni-based catalysts. The dehydration of 3-methylcyclohexanol to methylcyclohexenes is catalyzed by the Lewis acid sites represented by coordinatively unsaturated cations of unreduced Ni, whose presence was detected by XPS and confirmed by DRIFTS of adsorbed pyridine.

As highlighted in Table 3, the product distribution is strongly dependent on the Ni particle size. For the catalysts with Ni particles size ≥ 9 nm, besides toluene and 3-methylcyclohexanone, a relatively high selectivity to phenol is observed. Decreasing the Ni particle size to 1 nm (1nmNi/SBA-15) leads to a continuous decrease in the selectivity to phenol and HYD products (3-methylcycloxanone, 3-methylcyclohexa-nol, methylcyclohexenes and methylcyclohexane), the ketone remaining as the main product. In contrast, the decrease in the selectivity to those products is accompanied by the increase in the selectivity to toluene. These results suggest that varying Ni particle sizes change the product distribution toward different reaction pathways. The decrease in the particle size shifts the reaction toward the hydrogenation of the carbonyl group of the tautomer, leading to the formation of toluene or even the direct deoxygenation of m-cresol.

It is interesting to note that in terms of type of support, comparing the 25nmNi/SiO$_2$ and 9nmNi/SBA catalysts, some differences in terms of activity and selectivity can be observed. Ni supported on SBA-15 presented higher conversion at same space time highlighting the higher activity of the catalyst supported on SBA-15. Indeed, as reported in Table 4, the total reaction rates are 60.0 and 30.9 mmol g_{Ni}^{-1} h^{-1} for 9nmNi/SBA and 25nmNi/SiO$_2$, respectively. Furthermore, selectivity to toluene was lower while selectivity to phenol was 2-fold higher on the 25nmNi/SiO$_2$ catalyst. These results indicate that Ni particles confined in the mesopores of a type SBA-15 silica are more active than Ni particles dispersed on commercial silica. Improvement of activity by using SBA-15 as a support of Ni based catalysts was already reported by Jang et al. for the HDO of anisole in liquid phase, such effect was attributed to the effect of the pore size and pore structure of mesoporous SBA-15 [44].

The total reaction rate constant and the ones calculated for each reaction pathway are listed in Table 4. The catalyst activity strongly increases with decreasing Ni particle size, as the total reaction rate of catalysts supported on SBA-15 increases by a factor of 6 when particles size decreases from 9 to 1 nm. This result thus clearly indicates that smaller Ni particles are much more active than larger one in the conversion of m-cresol. Concerning the reaction rates for each reaction pathway, the DDO rate significantly increases by decreasing Ni particle size (around 10 times from 9 to 1 nm). On the contrary, HYD and HYG rates present only slight increases while the particles size decreases. The TOF values (Fig. 6) followed the same order as the reaction rate constants. The TOF for DDO increases from 23.6 to 70.1 h^{-1} when decreasing Ni particle size from 9 to 1 nm, clearly indicating that the intrinsic activity of smaller Ni particles is higher than the one of larger particles for the DDO route.

3.3. Effect of Ni particle size on surface site concentration and its relationship with catalytic activity

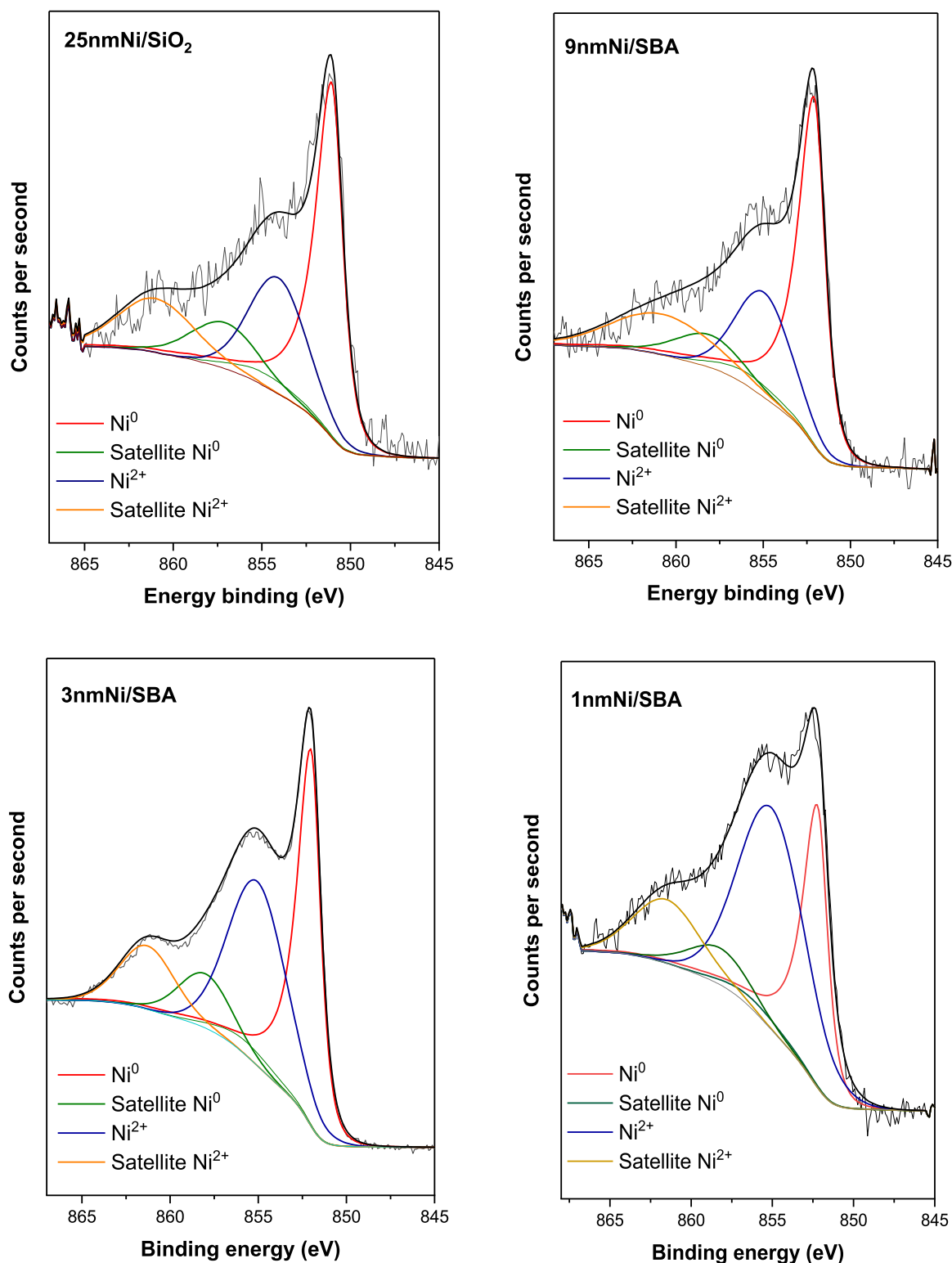The variation of the metal particle size can affect the reaction

Fig. 5. XP spectra of Ni2p core level for the Ni-based catalysts.

mechanism as observed in several catalytic reactions [37,54–57]. However, very few works are dedicated to this aspect for the HDO reaction, while several works have investigated the effect of metal type for the HDO of phenolic compounds. Experimental and theoretical studies showed that the HDO activity correlates directly with the metal oxophilicity [13,52,58]. According to Duong et al. [57] metal oxophilicity depends on the position of the d-band center relative to the Fermi level which in turn is affected by (i) the type of metal, and (ii) the extent of

coordination of the metal atoms. To demonstrate the second factor in the HDO activity, experimental and theoretical studies of Rh/SiO$_2$ catalysts with different Rh particle size (2 and 4 nm) for the HDO of m-cresol at gas phase (285 °C, 1 atm) were conducted. It was demonstrated that Rh/SiO$_2$ with small Rh(0) particles, thus containing more low-coordination sites such as step, is 1.7 times more active to the formation of toluene than a catalyst with larger particles (more high-coordination sites such as terrace). Yang et al. [37] further reported

Table 2

Binding energies of Ni 2p and atomic percentage of Ni species obtained from the curve-fitted values of XP spectra and acidic properties of the Ni-based catalysts after in situ reduction under pure hydrogen at 500 °C, 1 h.

Catalyst	Binding energy (eV)		Atomic composition (%)		Ni (0)/ Ni (II)	Acid sites distribution (μmol g^{-1})Lewis
	Ni (0)	Ni (II)	Ni (0)	Ni (II)		
25nmNi/ SiO$_2$	851.8	854.8	60	40	1.5	1
9nmNi/ SBA	852.1	855.2	55	45	1.2	25
3nmNi/ SBA	852.0	855.2	52	48	1.1	16
1nmNi/ SBA	852.2	855.3	39	61	0.6	38

a similar study using Ni supported on SiO$_2$ varying Ni particle size (2–22 nm) for the HDO of m-cresol (gas phase, 300 °C, 1 atm). The results showed that decreasing the Ni particle size improved the intrinsic reaction rate of HDO by 24 times with deoxygenation activity increasing while hydrogenation and hydrogenolysis activity decreased. By using DFT calculations, the authors examined the adsorption and deoxygenation of phenol on Ni(111), Ni(211) and defected Ni(211) surfaces, in order to simulate particles having sites (terrace, step and corner,

respectively) of different proportions. The adsorption energy of phenol followed the order: -116.7 kJ mol^{-1} on Ni (111) > -159.1 kJ mol^{-1} on Ni (211) > -194.8 kJ mol^{-1} on the defected Ni(211). Besides that, the activation and reaction energy decreased in the same order, thus demonstrating that corner type sites interact strongly with the oxygenated compound thus favoring the deoxygenation pathway. These finds are in agreement with Duong et al., and thus demonstrated that a highly coordinately unsaturated surface of Ni, represented by step and corner sites presented in small particles, is responsible for C-O bond cleavage affording the production of toluene. However, DFT calculations are not always readily available, which make interesting the search for simpler and effective methods to evaluate theoretical investigations.

In our work, in order to explain the effect of Ni particle size for m-cresol conversion, we proposed the use of a geometric model developed by Le Valant et al. [59] (denoted thereafter LV model), based on the
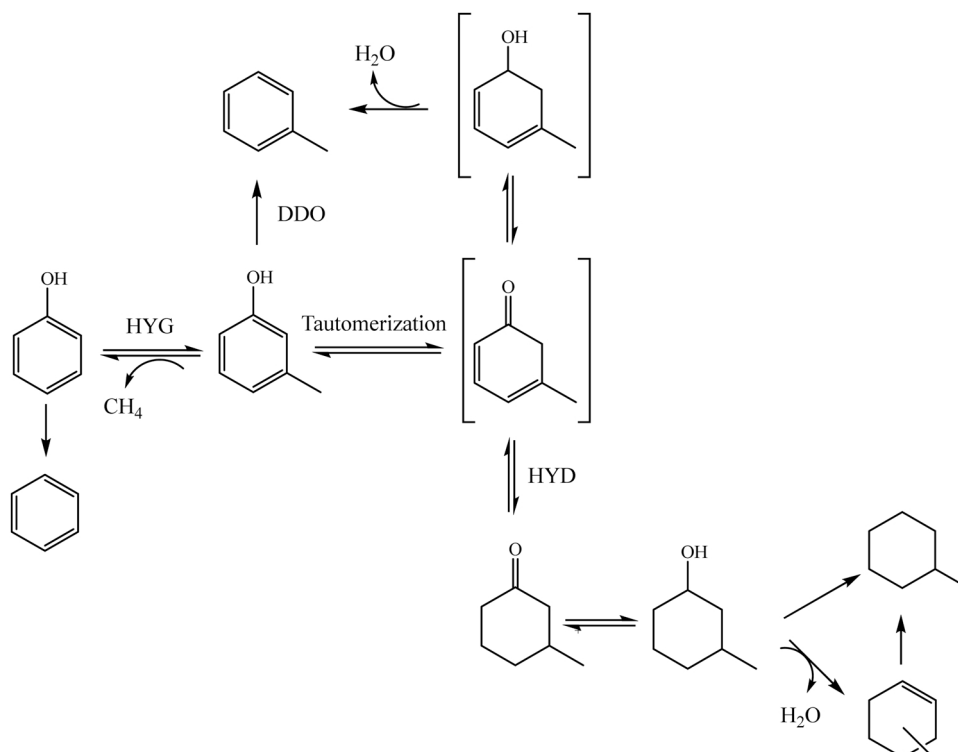
Table 4

Reaction rate constant (in mmol g$_{Ni}^{-1}$ h^{-1}) values calculated for the whole transformation of m-cresol and for each reaction pathway over Ni-based catalysts (300 °C, atmospheric pressure).

Catalyst	k_{TOT}	k_{DDO}	k_{HYD}	k_{HYG}
25nmNi/SiO$_2$	30.9	14.4	9.3	8.2
9nmNi/SBA	60.0	33.7	17.9	8.4
3nmNi/SBA	208.8	136.8	57.9	14.0
1nmNi/SBA	388.9	333.3	28.4	27.2

Table 3

Product distribution obtained in the transformation of m-cresol over the Ni-based catalysts (T$_{reduction}$ = 500 °C, T$_{reaction}$ = 300 °C, 1 atm, 0.5 h of TOS).

Catalyst	W/F (g h mol^{-1})	Conversion (%)	Selectivity (%)					Ph	Bz
			TOL	m-ONE	m-OL	m-ENES	m-ANE		
25nmNi/SiO$_2$	62	17.5	46.0	16.5	1.9	7.3	2.7	22.5	3.1
9nmNi/SBA	62	29.9	56.4	22.3	4.0	2.5	0.4	11.9	2.5
3nmNi/SBA	26	26.6	65.4	21.0	4.2	1.5	1.1	5.0	1.8
1nmNi/SBA	8	22.3	85.7	5.5	0.8	0.5	0.6	2.3	4.6

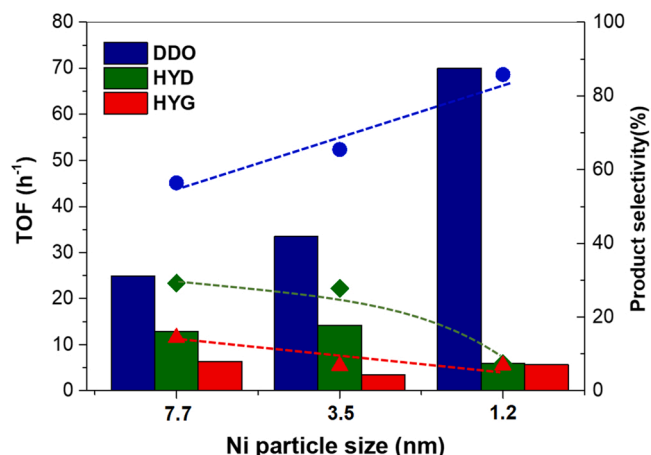**Scheme 1.** Reaction pathways proposed for the HDO of m-cresol over Ni-based catalysts.

Fig. 6. TOF values and selectivity of the products obtained from each reaction pathway as a function of Ni particle size. Bar graphs correspond to TOF values. Selectivity is represented by the dashed lines.

perfect truncated octahedron shape, to allow the quantification of surface site concentrations [corner, edge, face (100) and face (111)] for any fcc metal particle size. The evolution of surface site concentrations versus Ni particle size using this model is presented in Fig. 7. For the smallest Ni particle size (d = 0.75 nm), the corner sites are the main sites present on the surface (8070.5 µmol g_{Ni}^{-1}). As the metal particle size increases, there is an obvious decrease on the concentration of corner sites in favor of the edge, face (100), and face (111) sites. One can see that the edge, face (111), and face (100) site concentrations reach a maximum value (2150.9, 2373.4 and 358.7 µmol g_{Ni}^{-1} respectively) with Ni particle size equal precisely to 1.25, 1.50 and 2.73 nm, respectively, whereas the corner concentration monotonously decreases.

Activity of heterogeneous catalysts depends on the amounts of chemisorbed molecules, which themselves depend on the amount of surface sites. In this sense, the surface site concentrations of Ni presented in (Fig. 7) can be seen as a picture of a metallic catalyst activity per gram of Ni. As demonstrated by Calle-Vallejo et al. [60,61], all the energy considerations are intrinsically linked to the geometry of the active site. Assuming that the chosen surface sites have the same energetics for adsorption (whatever the Ni particle size), and the adsorbed molecules
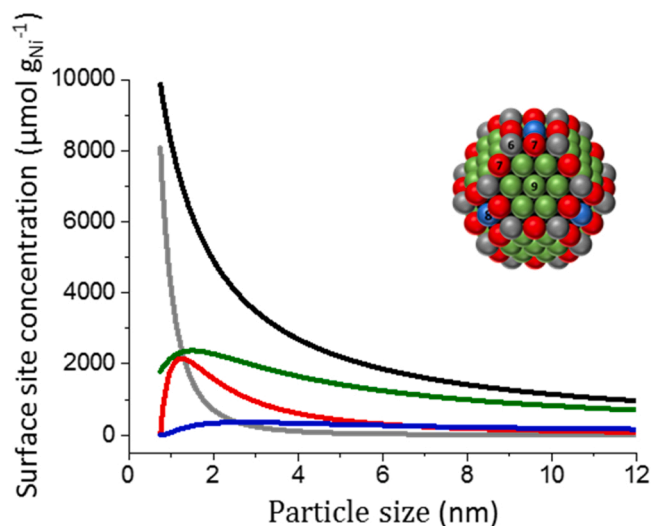

Fig. 7. Evolution of the surface site concentration of Ni in function of the particle size for a fcc perfect truncated octahedron (black: all sites; gray: corners; red: edges; blue: faces (100) and green: faces (111); with d_{Ni}= 0.249 nm, M_{Ni}= 58.693 g mol^{-1}).

do not interact with each other, the activity (denoted k_i) can then be expressed as a function of the surface site concentration (denoted [*site*] and determined using the LV model) by Eq. (5).

$$k_i = f([site]) \qquad (5)$$

Where i = total, DDO, HYD or HYG.

To validate this hypothesis, we compared the evolution of the normalized activity (denoted k_i^{norm}, determined using the Eq. (6) with the normalized surface site concentration (denoted $[site]^{norm}$, determined with the Eq. (7) as a function of the particle size.

$$k_i^{norm} = \frac{k_i}{k_i^{ref}} \qquad (6)$$

$$[site]^{norm} = \frac{[site]}{[site]^{ref}} \qquad (7)$$

Where k_i^{ref} represents the reference activity corresponding to the 1nmNi/SBA catalyst (333.3, 28.4, 27.2 and 388.9 mmol g_{Ni}^{-1} h^{-1} for k_{DDO}, k_{HYD}, k_{HYG} and k_{total}, respectively), and $[site]^{ref}$ corresponds to the reference surface site concentrations associated with the particle size of this catalyst, i.e. $\bar{d}$ = 1.2 nm (see the values in Table S2 gathering the surface site concentrations calculated as a function of the particle diameter).

The evolution of normalized activities (k_{DDO}^{norm}, k_{HYD}^{norm} and k_{HYG}^{norm}) and normalized surface site concentrations (all sites (Figs. S3–5a), corner (Figs. S3–5b), edge (Figs. S3–5c), face (100) (Figs. 3–5d), face (111) (Figs. S3–5e) versus the particle size are presented in Figs. S3–5. The best correlations between the experimental values of activity and the surface site concentration predicted by the model are obtained for the [Edge], [Face 100] and [Face 111] concentrations, for k_{DDO}^{norm}, k_{HYD}^{norm} and k_{HYG}^{norm} (Fig. 8), respectively. The evolutions of the three activities, k_{DDO} and k_{HYD}, and k_{HYG} scale linearly with the [Edge], [Face 100] and [Face 111] surface site concentrations, respectively (with an interception to zero (see Figs. S3–5f)). Thus, these results clearly evidence that the conversion of m-cresol is a structure sensitive reaction on Ni catalysts, and the model predict that the direct deoxygenation is favored on edges and corner type sites while hydrogenation and hydrogenolysis over face type sites. These results are in agreement with the DFT calculations performed by Yang et al. which demonstrated that the energy barrier for the deoxygenation of phenol over on Ni(111), Ni(211) and defect Ni(211) (used to simulate terrace, step and corner sites, respectively) decreased from 175.6 to 145.6 and to 120.5 kJ mol^{-1}, respectively, i.e. highly coordinatively unsaturated Ni sites, such as steps and corners, stabilize the adsorbed -OH group in the transition state, facilitating its deoxygenation [31]. Therefore, our model can be successfully used to correlate catalyst-properties with activity in the HDO reaction.

3.4. Catalyst stability

When the HDO reaction is performed under atmospheric pressure, catalysts are observed to deactivate during the first hours of reaction [8,15]. Then, the stability of the catalysts was investigated during 6 h of time on stream (TOS) at the same level of conversion (~ 50 %), 6 h being sufficient to obtain stable conversion and selectivities. Due to the lower activity of 25 nmNi/SiO$_2$ catalyst, a maximum of around 30 % of conversion was obtained. Fig. 9 shows the evolution of m-cresol conversion and the selectivity to products with TOS. For all catalysts, the conversion continuously decreases with time (around 18 % for 25nmNi/SiO$_2$, 9nmNi/SBA and 3nmNi/SBA catalysts, and 27 % for 1nmNi/SBA). Following the decrease in conversion, the yield of the main product (toluene) continuously decreases, with a slight increase in the yield of 3-methylcyclohexanone for the 9nmNi/SBA and 3nmNi/SBA catalysts (Fig. S6). A detailed analysis of the changes in the formation of products is made through the evolution of products selectivity with TOS
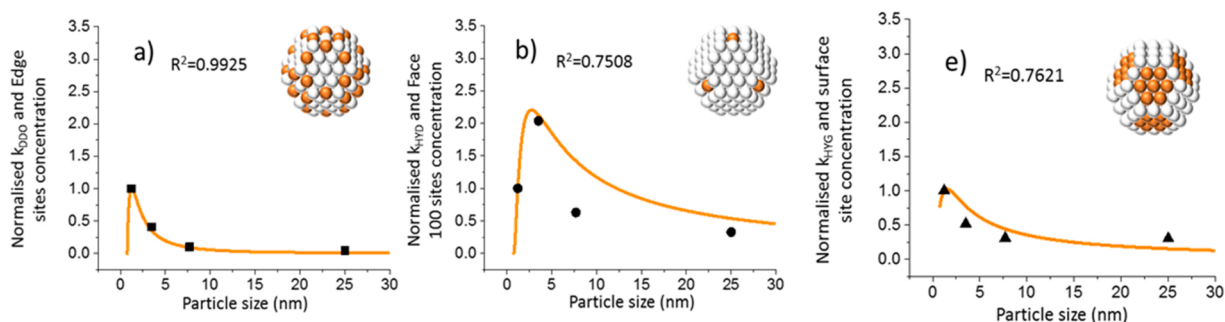
Fig. 8. The evolution of activity for the different reaction pathways (symbols) normalized by surface site concentration (orange curves) with Ni particle size: a) k_{DDO} (with predicted sites: edge); b) k_{HYD} (with predicted sites: face 100) and e) k_{HYG} (with predicted sites: face 111). Orange curves: results predicted with the model by using the following particle size values for the normalization: d= 1.2 nm for 1nmNi/SBA catalyst (with d_{Ni}= 0.249 nm, M_{Ni}= 58.693 g mol^{-1}).
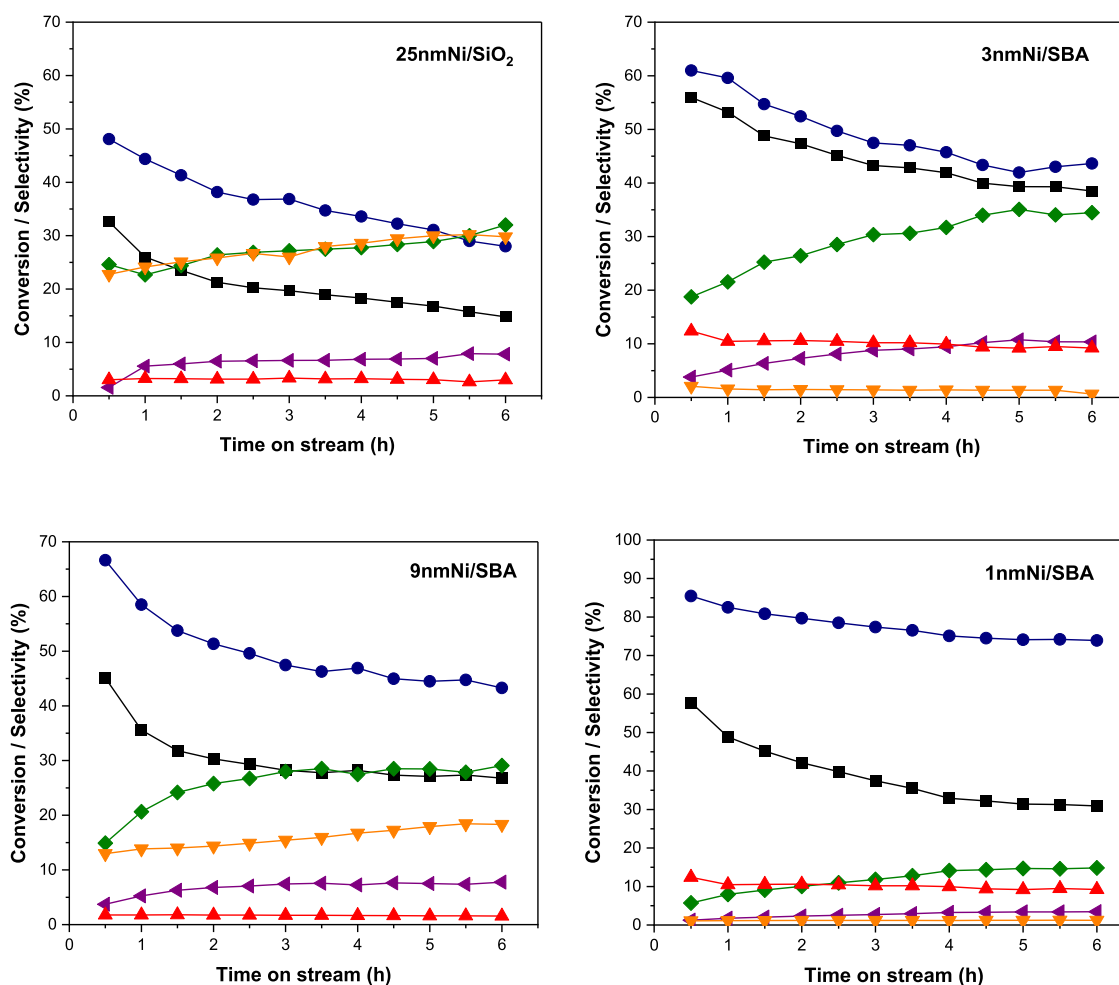

Fig. 9. Effect of time on stream on the m-cresol conversion and products yield over the Ni-based catalysts. T: 300 °C; P: 1 atm; H$_2$/m-cresol: 90; TOS: 6 h. (■) conversion, (●) toluene, (◆) 3-methylcyclohexanone, (◄) 3-methylcyclohexanol, (▲) methylcyclohexenes + methylcyclohexane, (▼) Phenol + benzene.

(Fig. 9). It is clearly observed that for the 25nmNi/SiO$_2$, 9nmNi/SBA and 3nmNi/SBA catalysts, the decrease in m-cresol conversion is accompanied by significant changes in the selectivity of main products. Selectivity to toluene continuously decreases while selectivity to 3-methylcyclohexanone and 3-methylcyclohexanol increases. Furthermore, for the catalysts containing larger Ni particles (25 nm/SiO$_2$ and 9nmNi/SBA), there was an important increase in the selectivity to phenol with TOS. Interestingly, for 1nmNi/SBA catalysts, in which a stronger drop in m-cresol conversion was observed, the changes in products selectivity were less significant. For example, the decrease in the selectivity to toluene followed the order: 25nmNi/SiO$_2$ (44 %) > 9nmNi/SBA (35 %) > 3nmNi/SBA (28 %) > 1nmNi/SBA (14 %).

Catalyst deactivation in HDO reaction is usually rationalized as a function of metal sintering and/or blockage of active sites by coke deposition or strong adsorption of reaction intermediates [5,8,9,15,16, 62–64]. Thus, TEM and XRD analysis were performed over the spent catalysts to verify if there was metal sintering, and ATG-MS analysis to investigate the formation of coke during reaction. The TEM images of spent 1nmNi/SBA catalyst (Fig. 10a) shows that the Ni particles are still confined in the pores of the support. However, the averaged Ni particles size (3–4 nm) is larger than that obtained for the reduced catalyst (1 nm), indicating that there was a significant sintering for this catalyst. For the 3nmNi/SBA, the majority of Ni particles with particle size around 3 nm are observed in the SBA pores, thus indicating a good resistance to sintering, however, it was identified some regions with the presence of larger particles inside or at the external surface of silica grains (range of 7–25 nm). Finally, for the 9nmNi/SBA catalyst, the average of Ni particles size was around 8–9 nm, suggesting that sintering does not occur during reaction over this catalyst. These observations are in accordance with the XRD of the spent catalysts (Fig. S7). For

1nmNi/SBA, the calculated crystalline size was 4 nm while for 3nmNi/SBA, no reflections are observed. For 25nmNi/SiO$_2$ and 9 nmNi/SBA, the calculated Ni crystallite size was 21 and 7 nm respectively, close to the initial particle sizes determined by TEM (25 and 7.7 nm respectively).

The TG profiles and MS signals with respect to CO$_2$ ($m/z = 44$) obtained during TG-MS analysis are presented in Fig. 11. The weight losses, quantified by TG analysis for the 25 nmNi/SiO$_2$, 9nmNi/SBA, 3nmNi/SBA and 1nmNi/SBA catalysts were 1.0; 6.4; 10.3 % and 8.5 % g/g$_{catalyst}$ respectively. The CO$_2$ evolution profile for 25nmNi/SiO$_2$ and 9nmNi/SBA showed a first small CO$_2$ production at 290 °C and a bigger CO$_2$ formation located between 400 °C and 600 °C (centred at 480 °C with a shoulder at 555 °C, in the case of 9nmNi/SBA). The peak at lower temperature may be due to the oxidation of adsorbed intermediate species on the catalyst surface, as previously reported [8,9]. The peak at higher temperature can be attributed to the combustion of condensed carbon deposits. Yang et al. tested Ni supported on silica catalysts for the HDO reaction of m-cresol, and they observed a high CO$_2$ production in
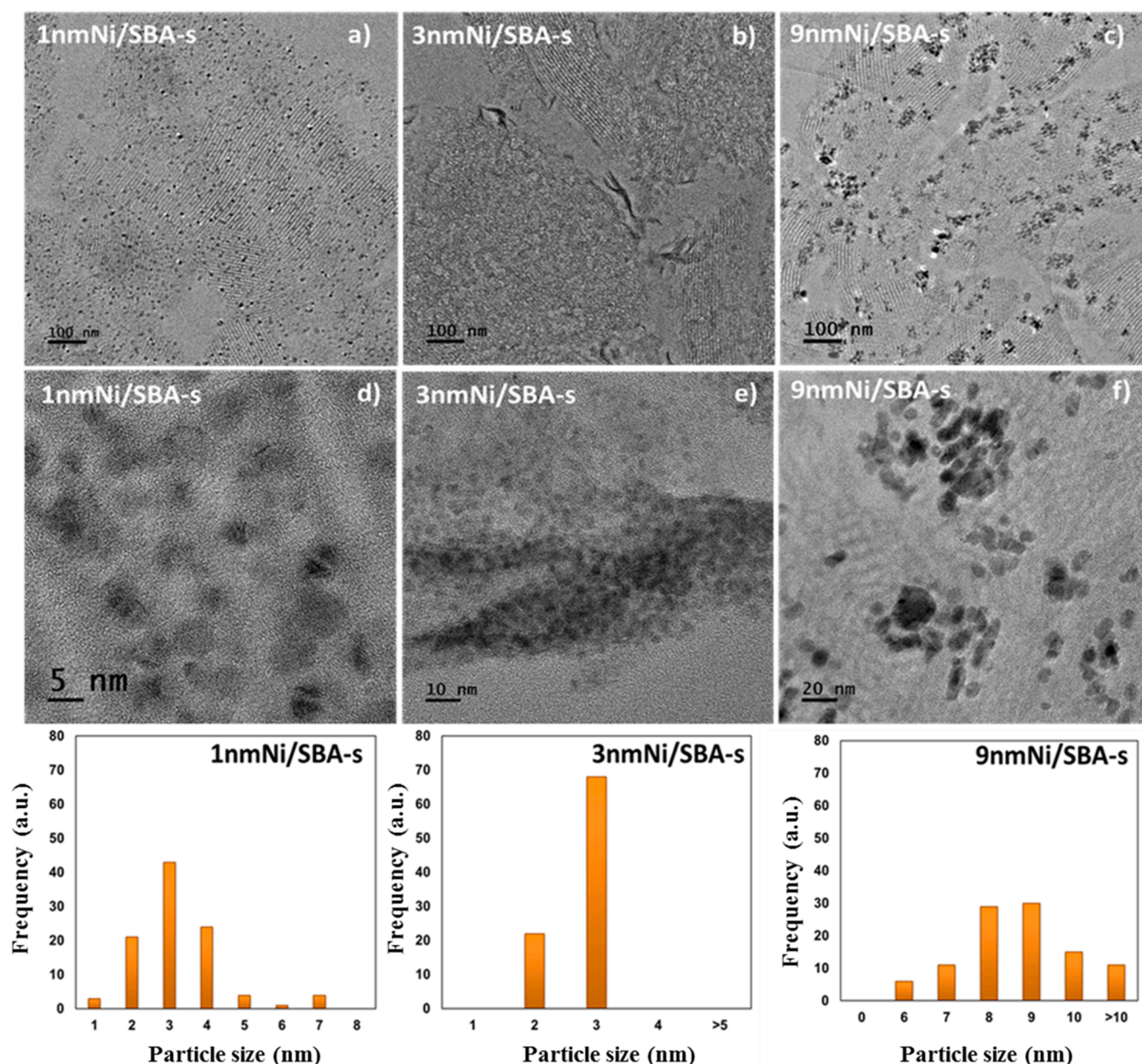

Fig. 10. Representative HR-TEM images of the post-reaction Ni supported on SBA catalysts.
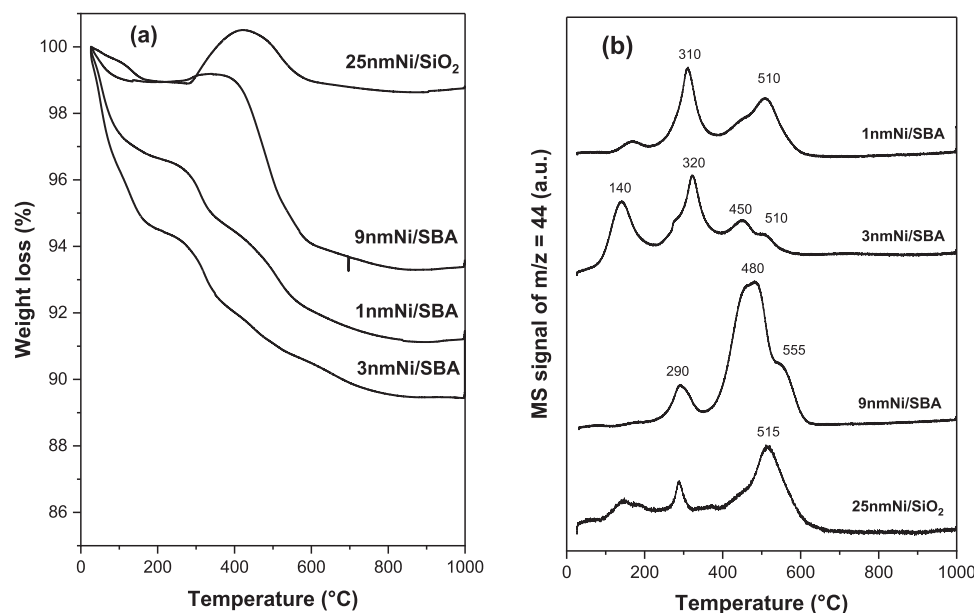
Fig. 11. TG profiles of spent catalysts after HDO reaction of m-cresol. MS signal of CO_2 during TG analysis. Note that the profiles have been normalized by weight of catalyst.

the same temperature region (506–548 °C) [62]. In our work, the differences observed in the TPO profiles of the catalysts can be correlated with the catalyst activity. For 25nmNi/SiO$_2$ and 9nmNi/SBA catalysts, which are more active for hydrogenolysis reaction, the carbon species on the Ni surface can originates from products of C-C hydrogenolysis reaction that may polymerize to a hydrogen-poor coke (thus combusted at higher temperatures). For the catalysts with lower Ni particle size, and thus less active for hydrogenolysis, m-cresol reacts and is faster desorbed from catalyst surface. As a result, intensity of the peaks located in the region of higher temperature (400–600 °C) for 3nmNi/SBA and 1nmNi/SBA are lower compared to the 25nmNi/SBA and 9nmNi/SBA catalysts. In their case, more significant evolution of CO_2 happens at lower temperatures (140 and 320 °C for 3nmNi/SBA and 310 °C for 1nmNi/SBA). Considering that smaller particles are more active for deoxygenation due to their higher oxophilicity, it is not surprising that intermediates oxygenated compounds strongly adsorb over the Ni particles, which explain the peaks at lower temperatures, thus avoiding these sites to further participate in the reaction. Therefore, the blockage of the active sites may be the major reason for catalyst deactivation, either through the deposit of coke or adsorption of intermediate species. However, metal sintering should also be considered in the case of the 1nmNi/SBA catalyst.

4. Conclusions

The present work investigated the reactivity of Ni particles confined in the pores of SBA-15 for the HDO of m-cresol in gas phase under atmospheric pressure. Different synthesis methods were used to control the Ni particle size and evaluate its effect on the reaction pathways involved in the conversion of m-cresol.

Ni nanoparticles in the range of 1–25 nm were obtained depending on the support and synthesis approach. The use of SBA-15 as a support allowed to confine Ni particles inside the channels thus limiting particle size to 9 nm instead 25 nm when supported on commercial SiO$_2$. By deposition-precipitation method and melt infiltration on the SBA-15 containing the porogen, very small Ni particles size were obtained, 3 and 1 nm respectively. The activity and the product distribution for the HDO of m-cresol significantly changed depending on the Ni particle size. Larger Ni particles (9–25 nm) favoured hydrogenation and hydrogenolysis reaction pathways yielding mainly methylcyclohexanone and

phenol, respectively, whereas smaller Ni particles (3 and 1 nm) are more active and promotes the deoxygenation pathway yielding toluene. Reducing Ni particle size from 9 to 1 nm increases the rate of the deoxygenation pathway by 10 times while 1.6 and 3.2 for hydrogenation and hydrogenolysis pathways. These findings were rationalized in terms of different type of sites: corner, edge, face. Face-type sites, present in higher concentration in larger particles (85 % of the sites at 8 nm) are more active for hydrogenation and hydrogenolysis, while decreasing the Ni particles size increases the concentration of edges and corners sites (83 % at 1 nm) sites which are more active for deoxygenation reaction. Also, particles confined into the mesoporosity of SBA-15 present a great resistance to sintering during reaction with catalyst deactivation being mainly caused by coke accumulation. Thus, this work demonstrates that efficient catalysts can be obtained by tuning metal particle size of transition metals, which may contribute to the design of more active and stable HDO catalysts.

CRediT authorship contribution statement

C. Abreu Teles: Investigation, Formal analysis, Validation, Writing – original draft. **C. Ciotonea:** Investigation, Formal analysis, Validation, Writing – original draft. **A. Le Valant:** Geometric model development, Review & Editing. **C. Canaff:** Formal analysis, Investigation. **Jérémy Dhainaut:** Formal analysis, Review & Editing. **Jean-Marc Clacens:** Review & Editing. **F. Bellot Noronha:** Conceptualization, Formal analysis, Writing – review & editing. **F. Richard:** Supervision, Conceptualization, Funding acquisition, Formal analysis, Writing – review & editing. **S. Royer:** Supervision, Conceptualization, Funding acquisition, Formal analysis, Writing – review & editing.

Declaration of Competing Interest

The authors declare that they have no known competing financial interests or personal relationships that could have appeared to influence the work reported in this paper.

Data availability

Data will be made available on request.

Acknowledgements

This work was performed in the frame of the PYRODEOX project granted by the ANR (ANR-21-CE43-0006). Camila A. Teles, Anthony Le Valant, Christine Canaff, Jean-Marc Clacens, and Frederic Richard acknowledge financial support from the European Union (ERDF), "Region Nouvelle Aquitaine". The Chevreul Institute is thanked for its help in the development of this work through the ARCHI-CM project supported by the "Ministère de l'Enseignement Supérieur de la Recherche et de l'Innovation", the region "Hauts-de-France", the ERDF program of the European Union and the "Métropole Européenne de Lille. Fabio B. Noronha thanks the Fundação de Amparo à Pesquisa do Estado do Rio de Janeiro (FAPERJ – E-26/202.783/2017), Conselho Nacional de Desenvolvimento Científico e Tecnologico (CNPq - 303667/2018-4; 305046/2015-2; 302469/2020-6) and the French government through the Programme Investissement d'Avenir (I-SITE ULNE / ANR-16-IDEX-0004 ULNE) managed by the Agence Nationale de la Recherche, CNRS, Métropole Européen de Lille (MEL) and Region Hauts-de-France for the financial support to "CatBioInnov" Project.

Appendix A. Supporting information

Supplementary data associated with this article can be found in the online version at doi:10.1016/j.apcatb.2023.123030.

References

[1] D.E. Resasco, S.P. Crossley, Implementation of concepts derived from model compound studies in the separation and conversion of bio-oil to fuel, Catal. Today 257 (2015) 185–199, https://doi.org/10.1016/j.cattod.2014.06.037.

[2] Y. Luo, V.K. Guda, E.B. Hassan, P.H. Steele, B. Mitchell, F. Yu, Hydrodeoxygenation of oxidized distilled bio-oil for the production of gasoline fuel type, Energy Convers. Manag. 112 (2016) 319–327, https://doi.org/10.1016/j.enconman.2015.12.047.

[3] A.S. Ouedraogo, P.R. Bhoi, Recent progress of metals supported catalysts for hydrodeoxygenation of biomass derived pyrolysis oil, J. Clean. Prod. 253 (2020), 119957, https://doi.org/10.1016/j.jclepro.2020.119957.

[4] A.J. Foster, P.T.M. Do, R.F. Lobo, The synergy of the support acid function and the metal function in the catalytic hydrodeoxygenation of M-Cresol, Top. Catal. 55 (3–4) (2012) 118–128, https://doi.org/10.1007/s11244-012-9781-7.

[5] X. Zhu, L. Nie, L.L. Lobban, R.G. Mallinson, D.E. Resasco, Efficient conversion of *m*-cresol to aromatics on a bifunctional Pt/Hbeta catalyst, Energy Fuels 28 (6) (2014) 4104–4111, https://doi.org/10.1021/ef500768r.

[6] M.B. Griffin, G.A. Ferguson, D.A. Ruddy, M.J. Biddy, G.T. Beckham, J.A. Schaidle, Role of the support and reaction conditions on the vapor-phase deoxygenation of *m*-cresol over Pt/C and Pt/TiO₂ catalysts, ACS Catal. 6 (4) (2016) 2715–2727, https://doi.org/10.1021/acscatal.5b02868.

[7] P.M. de Souza, R.C. Rabelo-Neto, L.E.P. Borges, G. Jacobs, B.H. Davis, T. Sooknoi, D.E. Resasco, F.B. Noronha, Role of Keto intermediates in the hydrodeoxygenation of phenol over Pd on oxophilic supports, ACS Catal. 5 (2) (2015) 1318–1329, https://doi.org/10.1021/cs501853t.

[8] C.A. Teles, P.M. de Souza, R.C. Rabelo-Neto, M.B. Griffin, C. Mukarakate, K. A. Orton, D.E. Resasco, F.B. Noronha, Catalytic upgrading of biomass pyrolysis vapors and model compounds using niobia supported Pd catalyst, Appl. Catal. B Environ. 238 (2018) 38–50, https://doi.org/10.1016/j.apcatb.2018.06.073.

[9] C.A. Teles, R.C. Rabelo-Neto, N. Duong, J. Quiroz, P.H.C. Camargo, G. Jacobs, D. E. Resasco, F.B. Noronha, Role of the metal-support interface in the hydrodeoxygenation reaction of phenol, Appl. Catal. B Environ. 277 (2020), 119238, https://doi.org/10.1016/j.apcatb.2020.119238.

[10] W. Song, Y. Liu, E. Baráth, C. Zhao, J.A. Lercher, Synergistic effects of Ni and acid sites for hydrogenation and C–O bond cleavage of substituted phenols, Green Chem. 17 (2) (2015) 1204–1218, https://doi.org/10.1039/C4GC01798F.

[11] Q. Xia, Z. Chen, Y. Shao, X. Gong, H. Wang, X. Liu, S.F. Parker, X. Han, S. Yang, Y. Wang, Direct hydrodeoxygenation of raw woody biomass into liquid alkanes, Nat. Commun. 7 (1) (2016) 11162, https://doi.org/10.1038/ncomms11162.

[12] Q. Sun, G. Chen, H. Wang, X. Liu, J. Han, Q. Ge, X. Zhu, Insights into the major reaction pathways of vapor-phase hydrodeoxygenation of *m*-cresol on a Pt/Hbeta catalyst, ChemCatChem 8 (3) (2016) 551–561, https://doi.org/10.1002/cctc.201501232.

[13] C.A. Teles, R.C. Rabelo-Neto, J.R. de Lima, L.V. Mattos, D.E. Resasco, F.B. Noronha, The effect of metal type on hydrodeoxygenation of phenol over silica supported catalysts, Catal. Lett. 146 (10) (2016) 1848–1857, https://doi.org/10.1007/s10562-016-1815-5.

[14] S. Kim, E.E. Kwon, Y.T. Kim, S. Jung, H.J. Kim, G.W. Huber, J. Lee, Recent advances in hydrodeoxygenation of biomass-derived oxygenates over heterogeneous catalysts, Green Chem. 21 (14) (2019) 3715–3743, https://doi.org/10.1039/C9GC01210A.

[15] C.A. Teles, R.C. Rabelo-Neto, G. Jacobs, B.H. Davis, D.E. Resasco, F.B. Noronha, Hydrodeoxygenation of phenol over zirconia-supported catalysts: the effect of metal type on reaction mechanism and catalyst deactivation, ChemCatChem 9 (14) (2017) 2850–2863, https://doi.org/10.1002/cctc.201700047.

[16] P.M. de Souza, R.C. Rabelo-Neto, L.E.P. Borges, G. Jacobs, B.H. Davis, D. E. Resasco, F.B. Noronha, Hydrodeoxygenation of phenol over Pd catalysts. Effect of support on reaction mechanism and catalyst deactivation, ACS Catal. 7 (3) (2017) 2058–2073, https://doi.org/10.1021/acscatal.6b02022.

[17] R.N. Olcese, M. Bettahar, D. Petitjean, B. Malaman, F. Giovanella, A. Dufour, Gas-phase hydrodeoxygenation of guaiacol over Fe/SiO2 catalyst, Appl. Catal. B Environ. 115–116 (2012) 63–73, https://doi.org/10.1016/j.apcatb.2011.12.005.

[18] X. Zhang, T. Wang, L. Ma, Q. Zhang, Y. Yu, Q. Liu, Characterization and catalytic properties of Ni and NiCu catalysts supported on ZrO2–SiO2 for guaiacol hydrodeoxygenation, Catal. Commun. 33 (2013) 15–19, https://doi.org/10.1016/j.catcom.2012.12.011.

[19] H. Fang, J. Zheng, X. Luo, J. Du, A. Roldan, S. Leoni, Y. Yuan, Product tunable behavior of carbon nanotubes-supported Ni–Fe catalysts for guaiacol hydrodeoxygenation, Appl. Catal. A Gen. 529 (2017) 20–31, https://doi.org/10.1016/j.apcata.2016.10.011.

[20] T.M. Sankaranarayanan, A. Berenguer, C. Ochoa-Hernández, I. Moreno, P. Jana, J. M. Coronado, D.P. Serrano, P. Pizarro, Hydrodeoxygenation of anisole as bio-oil model compound over supported ni and co catalysts: effect of metal and support properties, Catal. Today 243 (2015) 163–172, https://doi.org/10.1016/j.cattod.2014.09.004.

[21] Y. Yang, G. Lv, L. Deng, B. Lu, J. Li, J. Zhang, J. Shi, S. Du, Renewable aromatic production through hydrodeoxygenation of model bio-oil over mesoporous Ni/SBA-15 and Co/SBA-15, Microporous Mesoporous Mater. 250 (2017) 47–54, https://doi.org/10.1016/j.micromeso.2017.05.022.

[22] V.O.O. Gonçalves, W.H.S.M. Talon, V. Kartnaller, F. Venancio, J. Cajaiba, T. Cabioc'h, J.-M. Clacens, F. Richard, Hydrodeoxygenation of M-cresol as a depolymerized lignin probe molecule: synergistic effect of NiCo supported alloys, Catal. Today 377 (2021) 135–144, https://doi.org/10.1016/j.cattod.2020.10.042.

[23] P.M. Mortensen, J.-D. Grunwaldt, P.A. Jensen, A.D. Jensen, Screening of catalysts for hydrodeoxygenation of phenol as a model compound for bio-oil, ACS Catal. 3 (8) (2013) 1774–1785, https://doi.org/10.1021/cs400266e.

[24] L. Nie, P.M. de Souza, F.B. Noronha, W. An, T. Sooknoi, D.E. Resasco, Selective conversion of M-cresol to toluene over bimetallic Ni–Fe catalysts, J. Mol. Catal. A Chem. 388–389 (2014) 47–55, https://doi.org/10.1016/j.molcata.2013.09.029.

[25] X. Liu, W. An, C.H. Turner, D.E. Resasco, Hydrodeoxygenation of M-cresol over bimetallic nife alloys: kinetics and thermodynamics insight into reaction mechanism, J. Catal. 359 (2018) 272–286, https://doi.org/10.1016/j.jcat.2018.01.006.

[26] Q. Han, M.U. Rehman, J. Wang, A. Rykov, O.Y. Gutiérrez, Y. Zhao, S. Wang, X. Ma, J.A. Lercher, The synergistic effect between Ni sites and Ni-Fe alloy sites on hydrodeoxygenation of lignin-derived phenols, Appl. Catal. B Environ. 253 (2019) 348–358, https://doi.org/10.1016/j.apcatb.2019.04.065.

[27] A. Aqsha, L. Katta, M.M. Tijani, C.F. Oliveira, N. Mahinpey, Investigation of catalytic hydrodeoxygenation of anisole as bio-oil model compound over Ni-Mo / TiO₂ and Ni-V / TiO₂ catalysts: synthesis, kinetic, and reaction pathways studies, Can. J. Chem. Eng. 99 (5) (2021) 1094–1106, https://doi.org/10.1002/cjce.23912.

[28] Y. Zhang, G. Fan, L. Yang, L. Zheng, F. Li, Cooperative effects between ni-mo alloy sites and defective structures over hierarchical Ni-Mo bimetallic catalysts enable the enhanced hydrodeoxygenation activity, ACS Sustain. Chem. Eng. 9 (34) (2021) 11604–11615, https://doi.org/10.1021/acssuschemeng.1c04762.

[29] W. Song, Y. Liu, E. Baráth, C. Zhao, J.A. Lercher, Synergistic effects of Ni and acid sites for hydrogenation and C–O bond cleavage of substituted phenols, Green Chem. 17 (2) (2015) 1204–1218, https://doi.org/10.1039/C4GC01798F.

[30] X. Zhao, X. Wu, H. Wang, J. Han, Q. Ge, X. Zhu, Effect of strong metal-support interaction of Pt/TiO₂ on hydrodeoxygenation of m-cresol, ChemistrySelect 3 (37) (2018) 10364–10370, https://doi.org/10.1002/slct.201801147.

[31] C. Newman, X. Zhou, B. Goundie, I.T. Ghampson, R.A. Pollock, Z. Ross, M. C. Wheeler, R.W. Meulenberg, R.N. Austin, B.G. Frederick, Effects of support identity and metal dispersion in supported ruthenium hydrodeoxygenation catalysts, Appl. Catal. A Gen. 477 (2014) 64–74, https://doi.org/10.1016/j.apcata.2014.02.030.

[32] S.M. Schimming, O.D. LaMont, M. König, A.K. Rogers, A.D. D'Amico, M.M. Yung, C. Sievers, Hydrodeoxygenation of guaiacol over ceria-zirconia catalysts, ChemSusChem 8 (12) (2015) 2073–2083, https://doi.org/10.1002/cssc.201500317.

[33] J. Zhang, J. Chen, S. Chen, Q. Hu, Z. Gao, Y. Li, Y. Qin, Highly dispersed Pt nanoparticles supported on carbon nanotubes produced by atomic layer deposition for hydrogen generation from hydrolysis of ammonia borane, Catal. Sci. Technol. 7 (2) (2017) 322–329, https://doi.org/10.1039/C6CY01960A.

[34] P.-J. Hsu, Y.-C. Lin, Hydrodeoxygenation of 4-methylguaiacol over silica-supported nickel phosphide catalysts: the particle size effect, J. Taiwan Inst. Chem. Eng. 79 (2017) 80–87, https://doi.org/10.1016/j.jtice.2017.02.020.

[35] Y.K. Lugo-José, J.R. Monnier, A. Heyden, C.T. Williams, Hydrodeoxygenation of propanoic acid over silica-supported palladium: effect of metal particle size, Catal. Sci. Technol. 4 (11) (2014) 3909–3916, https://doi.org/10.1039/C4CY00605D.

[36] Size-Dependent Strong Metal–Support Interactions of Rutile.Pdf.

[37] F. Yang, D. Liu, Y. Zhao, H. Wang, J. Han, Q. Ge, X. Zhu, Size dependence of vapor phase hydrodeoxygenation of *m*-cresol on Ni/SiO₂ catalysts, ACS Catal. 8 (3) (2018) 1672–1682, https://doi.org/10.1021/acscatal.7b04097.

[38] P.M. Mortensen, J.-D. Grunwaldt, P.A. Jensen, A.D. Jensen, Influence on nickel particle size on the hydrodeoxygenation of phenol over Ni/SiO 2, Catal. Today 259 (2016) 277–284, https://doi.org/10.1016/j.cattod.2015.08.022.

[39] H. Vargas-Villagrán, M.A. Flores-Villeda, I. Puente-Lee, D.A. Solís-Casados, A. Gómez-Cortés, G. Díaz-Guerrero, T.E. Klimova, Supported nickel catalysts for anisole hydrodeoxygenation: increase in the selectivity to cyclohexane, Catal. Today 349 (2020) 26–41, https://doi.org/10.1016/j.cattod.2018.07.057.

[40] S. Lin, L. Shi, M.M.L. Ribeiro Carrott, P.J.M. Carrott, J. Rocha, M.R. Li, X.D. Zou, Direct synthesis without addition of acid of Al-SBA-15 with controllable porosity and high hydrothermal stability, Microporous Mesoporous Mater. 142 (2–3) (2011) 526–534, https://doi.org/10.1016/j.micromeso.2010.12.043.

[41] A. Berenguer, T.M. Sankaranarayanan, G. Gómez, I. Moreno, J.M. Coronado, P. Pizarro, D.P. Serrano, Evaluation of transition metal phosphides supported on ordered mesoporous materials as catalysts for phenol hydrodeoxygenation, Green Chem. 18 (7) (2016) 1938–1951, https://doi.org/10.1039/C5GC02188J.

[42] A. Ungureanu, B. Dragoi, V. Hulea, T. Cacciaguerra, D. Meloni, V. Solinas, E. Dumitriu, Effect of aluminium incorporation by the "PH-Adjusting" method on the structural, acidic and catalytic properties of mesoporous SBA-15, Microporous Mesoporous Mater. 163 (2012) 51–64, https://doi.org/10.1016/j.micromeso.2012.05.007.

[43] C. Ciotonea, B. Dragoi, A. Ungureanu, C. Catrinescu, S. Petit, H. Alamdari, E. Marceau, E. Dumitriu, S. Royer, Improved dispersion of transition metals in mesoporous materials through a polymer-assisted melt infiltration method, Catal. Sci. Technol. 7 (22) (2017) 5448–5456, https://doi.org/10.1039/C7CY00963A.

[44] C. Ciotonea, N. Hammi, J. Dhainaut, M. Marinova, A. Ungureanu, A. El Kadib, C. Michon, S. Royer, Phyllosilicate-derived nickel-cobalt bimetallic nanoparticles for the catalytic hydrogenation of imines, oximes and N-heteroarenes, ChemCatChem 12 (18) (2020) 4652–4663, https://doi.org/10.1002/cctc.202000704.

[45] M. Kruk, M. Jaroniec, A. Sayari, Application of large pore MCM-41 molecular sieves to improve pore size analysis using nitrogen adsorption measurements, Langmuir 13 (23) (1997) 6267–6273, https://doi.org/10.1021/la970776m.

[46] M. Thommes, K. Kaneko, A.V. Neimark, J.P. Olivier, F. Rodriguez-Reinoso, J. Rouquerol, K.S.W. Sing, Physisorption of gases, with special reference to the evaluation of surface area and pore size distribution (IUPAC technical report, Pure Appl. Chem. 87 (9–10) (2015) 1051–1069, https://doi.org/10.1515/pac-2014-1117.

[47] R.J. Madon, M. Boudart, Experimental criterion for the absence of artifacts in the measurement of rates of heterogeneous catalytic reactions, Ind. Eng. Chem. Fund. 21 (4) (1982) 438–447, https://doi.org/10.1021/i100008a022.

[48] C. Ciotonea, B. Dragoi, A. Ungureanu, A. Chirieac, S. Petit, S. Royer, E. Dumitriu, Nanosized transition metals in controlled environments of phyllosilicate–mesoporous silica composites as highly thermostable and active catalysts, Chem. Commun. 49 (69) (2013) 7665, https://doi.org/10.1039/c3cc43197e.

[49] S. Chen, C. Ciotonea, A. Ungureanu, E. Dumitriu, C. Catrinescu, R. Wojcieszak, F. Dumeignil, S. Royer, Preparation of nickel (oxide) nanoparticles confined in the secondary pore network of mesoporous scaffolds using melt infiltration, Catal. Today 334 (2019) 48–58, https://doi.org/10.1016/j.cattod.2019.01.064.

[50] P. Burattin, M. Che, C. Louis, Characterization of the Ni(II) phase formed on silica upon deposition−precipitation, J. Phys. Chem. B 101 (36) (1997) 7060–7074, https://doi.org/10.1021/jp970194d.

[51] V.O.O. Gonçalves, P.M. de Souza, T. Cabioc'h, V.T. da Silva, F.B. Noronha, F. Richard, Hydrodeoxygenation of M-cresol over nickel and nickel phosphide based catalysts. influence of the nature of the active phase and the support, Appl. Catal. B Environ. 219 (2017) 619–628, https://doi.org/10.1016/j.apcatb.2017.07.042.

[52] Q. Tan, G. Wang, L. Nie, A. Dinse, C. Buda, J. Shabaker, D.E. Resasco, Different product distributions and mechanistic aspects of the hydrodeoxygenation of m-cresol over platinum and ruthenium catalysts, ACS Catal. 5 (11) (2015) 6271–6283, https://doi.org/10.1021/acscatal.5b00765.

[53] J. Lee, Y. Xu, G.W. Huber, High-throughput screening of monometallic catalysts for aqueous-phase hydrogenation of biomass-derived oxygenates, Appl. Catal. B Environ. 140–141 (2013) 98–107, https://doi.org/10.1016/j.apcatb.2013.03.031.

[54] F. Jiang, F. Cai, B. Liu, Y. Xu, X. Liu, Particle size effects in the selective hydrogenation of cinnamaldehyde over supported palladium catalysts, RSC Adv. 6 (79) (2016) 75541–75551, https://doi.org/10.1039/C6RA17000E.

[55] A.L.M. da Silva, J.P. den Breejen, L.V. Mattos, J.H. Bitter, K.P. de Jong, F. B. Noronha, Cobalt particle size effects on catalytic performance for ethanol steam reforming – smaller is better, J. Catal. 318 (2014) 67–74, https://doi.org/10.1016/j.jcat.2014.07.020.

[56] M. Kourtelesis, P. Panagiotopoulou, X.E. Verykios, Influence of structural parameters on the reaction of low temperature ethanol steam Reforming over Pt/Al2O3 catalysts, Catal. Today 258 (2015) 247–255, https://doi.org/10.1016/j.cattod.2014.12.035.

[57] N. Duong, Q. Tan, D.E. Resasco, Controlling phenolic hydrodeoxygenation by tailoring metal–O bond strength via specific catalyst metal type and particle size selection, C. R. Chim. 21 (3–4) (2018) 155–163, https://doi.org/10.1016/j.crci.2017.07.008.

[58] Q. Tan, G. Wang, A. Long, A. Dinse, C. Buda, J. Shabaker, D.E. Resasco, Mechanistic analysis of the role of metal oxophilicity in the hydrodeoxygenation of anisole, J. Catal. 347 (2017) 102–115, https://doi.org/10.1016/j.jcat.2017.01.008.

[59] A. Le Valant, S. Bouchet, A. Van Assche, C. Especel, F. Epron, Description of supported metal structure sensitivity by a geometric approach, J. Catal. 397 (2021) 64–74, https://doi.org/10.1016/j.jcat.2021.03.021.

[60] F. Calle-Vallejo, D. Loffreda, M.T.M. Koper, P. Sautet, Introducing structural sensitivity into adsorption–energy scaling relations by means of coordination numbers, Nat. Chem. 7 (5) (2015) 403–410, https://doi.org/10.1038/nchem.2226.

[61] Calle-Vallejo, F., Tymoczko, J., Colic, V., Vu, Q.H., Pohl, M.D., Morgenstern, K., Loffreda, D., Sautet, P., Schuhmann, W., Bandarenka, A.S. Finding Optimal Surface Sites on Heterogeneous Catalysts by Counting Nearest Neighbors. 6.

[62] F. Yang, H. Wang, J. Han, Q. Ge, X. Zhu, Influence of Re addition to Ni/SiO2 catalyst on the reaction network and deactivation during hydrodeoxygenation of m-cresol, Catal. Today 347 (2020) 79–86, https://doi.org/10.1016/j.cattod.2018.04.073.

[63] P. Yan, M. Drewery, J. Mensah, J.C. Mackie, E. Kennedy, M. Stockenhuber, Study on catalyst deactivation during the hydrodeoxygenation of model compounds, Top. Catal. 63 (9–10) (2020) 778–792, https://doi.org/10.1007/s11244-020-01310-2.

[64] X. Lan, E.J.M. Hensen, T. Weber, Hydrodeoxygenation of guaiacol over Ni2P/SiO2–reaction mechanism and catalyst deactivation, Appl. Catal. A Gen. 550 (2018) 57–66, https://doi.org/10.1016/j.apcata.2017.10.018.